

VIBRATION CONTROL AND GUST ALLEVIATION
OF HIGHLY FLEXIBLE BLENDED-WING-BODY
AIRCRAFT

by

PETER ANTHONY CHIEGO

WEIHUA SU, COMMITTEE CHAIR

JINWEI SHEN

STEVE SHEPARD

A THESIS

Submitted in partial fulfillment of the requirements
for the degree of Master of Science
in the Department of Aerospace Engineering
in the Graduate School of
The University of Alabama

TUSCALOOSA, ALABAMA

2019

Copyright Peter Anthony Chiego 2019
ALL RIGHTS RESERVED

ABSTRACT

Suppressing the excitation from gusts that flexible vehicles experience in high-altitude, long-endurance flights is critical to improving their flight performance and maintaining stable flight. Aircraft designed for high-altitude, long-endurance flights tend to be more flexible due to the design requirements of their missions. The aircraft may experience external disturbances such as gusts throughout their flights which can cause large deformations in the flexible, lightweight wings. These disturbances can potentially excite unstable modes within the flexible aircraft, depending on the flight speed and gust strength. In this thesis the open-loop and closed-loop dynamic responses of a blended-wing-body aircraft subjected to different gust profiles are examined. Three flight speeds are considered: nominal, pre-flutter, and post-flutter. An LQR controller is then designed and implemented to examine the closed-loop dynamic responses of these same flight profiles. It is found that the controller is able to suppress vibration and wing root loading as well as delay the onset of unstable behavior.

DEDICATION

To my friends and family.

LIST OF SYMBOLS

p_B	Rigid-body position of aircraft
θ_B	Rigid-body orientation of aircraft
v_B	Rigid-body velocity of aircraft
ω_B	Rigid-body angular velocity of aircraft
ε_e	Elemental strain vector
ε_x	Extension strain
k_x	Twist strain
k_y	Out-of-plane bending strain
k_z	In-plane bending strain
M	Components of generalized inertia matrix
B	Body frame
B	Influence matrix for control loads
CFF	Components of generalized damping matrix
CFB	Components of generalized damping matrix
CBF	Components of generalized damping matrix
K	Generalized stiffness matrix
R	Generalized loads
J	Jacobian matrices
λ	Inflow states for unsteady aerodynamics
ζ	Quaternions
C^{GB}	Rotation matrix from global to body frame
ρ_∞	Air density

- lmc* Aerodynamic lift in local aerodynamic frame
- mmc* Aerodynamic moment in local aerodynamic frame
- dmc* Aerodynamic drag in local aerodynamic frame
- U_∞ Flight speed
- δ Elevator deflection
- F1,** Matrices for inflow states differential equation
- F2,** Matrices for inflow states differential equation
- F3** Matrices for inflow states differential equation
- Q** Weighting matrix for state inputs
- R** Weighting matrix for control inputs
- k** Gain matrix for controller

ACKNOWLEDGMENTS

I am extremely grateful for the guidance of my advisor Dr. Weihua Su. Without his help and wisdom, I would not have been able to complete this thesis and take the next step in my life. I would also like to thank my committee members Dr. Jinwei Shen and Dr. Steve Shepard for being apart of this process. Finally, I am thankful for the support that Dr. Paul Hubner has provided throughout my undergraduate and graduate career at The University of Alabama.

CONTENTS

ABSTRACT	ii
DEDICATION.....	iii
LIST OF SYMBOLS	iv
ACKNOWLEDGMENTS	vi
LIST OF FIGURES.....	ix
1 INTRODUCTION	1
1.1 Background and Motivation	1
2 METHODOLOGY.....	5
2.1 Aeroelastic Equations	5
2.1.1 Reference Frames	5
2.1.2 Elements with Constant Strain	8
2.1.3 Equations of Motion	8
2.1.4 Unsteady Aerodynamics.....	10
2.1.5 Controller Design	11
2.1.6 Aircraft Model.....	15
2.1.7 Gust Model	18
3 DYNAMIC RESPONSE	20
3.1 Discrete Gust (1-cosine)	20
3.1.1 90 m/s.....	20
3.1.2 110 m/s.....	24
3.1.3 120 m/s.....	28
3.2 Continuous Gust – Dryden.....	34
3.2.1 90 m/s.....	34

3.2.2	110 m/s.....	38
3.2.3	120 m/s.....	43
3.3	No Gust – Post Flutter	48
3.3.1	120 m/s.....	49
3.3.2	125 m/s.....	53
4	CONCLUSION AND FUTURE WORK.....	57
4.1	Conclusions	57
4.2	Future Work / Recommendations	58
	REFERENCES	59

LIST OF FIGURES

2.1	Body and global frame for rigid-body motion	6
2.2	Flexible lifting-surfaces frames within the body frame	7
2.3	Airfoil coordinate systems and velocity components	10
2.4	Block diagram of control scheme.....	13
2.5	Geometry of Blended-Wing-Body aircraft	16
2.6	Root locus plot with increasing velocities	17
2.7	Zoomed in root locus plot	18
3.1	Pitch Angle for discrete gust at 90m/s	21
3.2	Tip displacement for discrete gust at 90m/s	22
3.3	Root bending moment for discrete gust at 90m/s	23
3.4	Outer elevator deflection for discrete gust at 90m/s	24
3.5	Pitch angle for discrete gust at 110m/s	25
3.6	Tip displacement for discrete gust at 110m/s	26
3.7	Root bending moment for discrete gust at 110m/s	27
3.8	Outer elevator deflection for discrete gust at 110m/s	28
3.9	Plunge for discrete gust at 120m/s	29
3.10	Pitch angle for discrete gust at 120m/s	30
3.11	Tip displacement for discrete gust at 120 m/s	31
3.12	Root bending moment for discrete gust at 120m/s	32
3.13	Outer elevator deflection for discrete gust at 120m/s	33
3.14	Pitch angle for continuous gust at 90m/s	35

3.15	Tip displacement for continuous gust at 90m/s	36
3.16	Root bending moment for continuous gust at 90m/s	37
3.17	Outer elevator deflection for continuous gust at 90m/s	38
3.18	Plunge for continuous gust at 110m/s	39
3.19	Pitch angle for continuous gust at 110m/s	40
3.20	Tip displacement for continuous gust at 110m/s	41
3.21	Root bending moment for continuous gust at 110m/s	42
3.22	Outermost elevator deflection for continuous gust at 110m/s	43
3.23	Plunge for continuous gust at 120m/s	44
3.24	Pitch angle for continuous gust at 120m/s	45
3.25	Tip displacement for continuous gust at 120m/s	46
3.26	Root bending moment for continuous gust at 120m/s	47
3.27	Outermost elevator deflection for continuous gust at 120m/s	48
3.28	Plunge for no gust at 120m/s	50
3.29	Tip displacement for no gust at 120m/s	51
3.30	Root bending moment for no gust at 120m/s	52
3.31	Outermost elevator deflection for no gust at 120m/s	53
3.32	Plunge for no gust at 125m/s	54
3.33	Tip displacement for no gust at 125m/s	55
3.34	Root bending moment for no gust at 125m/s	56

1 INTRODUCTION

1.1 Background and Motivation

Although the concept of a blended wing body aircraft has been around since before World War II, production has been limited. A cross between conventional aircraft and a flying wing, the blended wing body aircraft design has inherent challenges for commercial applications despite certain practical advantages. Commercial infrastructure airports are designed for conventional tube-and-wing aircraft and may be unable to support larger span blended wing bodies. The current container loading, runways, taxiways, and terminals would have difficulties accommodating the unorthodox design. However due to the design of the blended wing body, the fuselage itself is able to contribute lift. This allows the entire aircraft to generate lift, resulting in a higher lift-to-drag ratio. This increases fuel economy at cruise conditions, making it ideal for long endurance flights. Despite commercial difficulties, the blended wing body design has been used in the military domain.

Over the past few decades, multiple blended wing body (BWB) aircrafts have been developed for high-altitude endurance missions for the military. One of the first in the late 1990's was the Lockheed Martin RQ-3 DarkStar, a fully autonomous UAV designed for reconnaissance. It featured a disk-shaped fuselage that contoured into its straight wings. Northrop's X-47A Pegasus came a few years later and sported delta wings

incorporated into a diamond shaped aircraft planform. More recently, Lockheed's RG-170 Sentinel features a design similar to the B-2 as well as the model used in this paper. The Sentinel is still in service carrying out reconnaissance missions for the Air Force.

Compared to standard tube-and-wing designs, the blended wing body and other aircrafts used for high-altitude, long endurance (HALE) missions tend to have lighter and more flexible wings. While necessary to conduct their mission, HALE aircrafts come with structural and aerodynamic challenges, especially when coupled. As seen in [15], the low frequency of the rigid body motion of these flexible aircrafts coupled with the low frequency bending modes can cause a body-freedom flutter phenomenon. This occurs when the rigid body motion of the aircraft, such as pitching, excites unstable modes within the wings of the aircraft. This would allow for the rigid body motion of the aircraft to excite flutter within the wings. When subjected to additional disturbances such as flying through a gust, these dangers can be amplified. These dangers have also been explored on a micro-vehicle [14] scale.

Investigating the aeroelastic effects that come from gusts on highly flexible vehicles has been looked at in a number of ways. It was shown by Su and Cesnik [10] that even at lower speeds, a finite gust perturbation could excite instability within the aircraft. They showed the need for some sort of control scheme to allow the HALE aircraft to successfully pass through atmospheric disturbances. Yagil [1] looked at trimming the vehicle with both leading and trailing edge flaps to minimize the structural deformation from the gust. They also examined a conventional trim configuration which was able to complete the trim of the aircraft, but unable to contain the deformation below the maximum allowed value. However, the model they examined was similar to the Helios Prototype which is designed

to allow larger wing deformations than the BWB. A control scheme was developed for the HALE aircraft [11] and shown to be successful in a nonlinear framework, but the BWB still needs to be examined.

Dillsaver, Cesnik, and Kolmanovsky [3] explored how a Linear Quadratic Gaussian (LQG) controller would be able to handle the gust alleviation. For an actual aircraft, an idealized control scheme may not be possible where all control surfaces are available for use so a Kalman filter would be required. However, artificial hair sensors have been used [9] as a way to get complete aircraft condition information. Their flight speed, 14 m/s, was an order of magnitude lower than what this paper uses. The effects of higher speeds on gust alleviation and flight dynamics still need to be explored.

Many studies have been conducted to test the feasibility of implementing a modern control system for the blended wing body. A Linear Quadratic Regulator (LQR) controller was shown to potentially be able to overcome longitudinal and lateral instabilities found within the BWB [4]. Although the authors used rudders as well for control surfaces in lateral stability, purely longitudinal behavior will be explored in this paper. Wildschek [5], however, showed that despite the potential to alleviate gusts through active stabilization, the power required in the elevators to do so exceeds the allowable loading passengers may experience in a commercial setting. While the commercial applications of a BWB will not be examined, it is worth noting that sensors on these crafts may have similar limitations. More robust control schemes have been developed as well, though not verified in a nonlinear framework. He et al. [12] developed a framework of linear parameter-varying modeling and control which was then applied to a blended wing body. They were able to control the instability while improving the performance of the aircraft. This paper will develop an LQR

controller and verify it within a nonlinear framework. The elevators of the BWB model in this thesis will be actuated to reduce the frequency of vibration within the aircraft by driving the controlled states back to their trimmed conditions.

2 METHODOLOGY

This thesis utilizes the UM/NAST aeroelastic toolbox from the University of Michigan to examine the dynamic response of the blended-wing-body aircraft. The underlying equations and methods used in this toolbox will be discussed, followed by the control theory used in developing the controller.

2.1 Aeroelastic Equations

Su et al. in [6] obtain solutions to the coupled aeroelastic and flight dynamic equations utilizing a strain-based nonlinear beam formulation. A brief overview of their method follows.

2.1.1 Reference Frames

A body frame must be defined for the aircraft's position and orientation. This body frame, B , is located within the global inertial frame G . Both the body and global frame are shown in Figure 2.1. The body frame defines $Bx(t)$ along the right wing and $By(t)$ towards the nose. $Bz(t)$ is defined as the cross product between the two pointing vertically up. From this frame the aircraft's position and orientation can be defined as

$$b = \begin{Bmatrix} p_B \\ \theta_B \end{Bmatrix} \quad (2.1)$$

$$\dot{b} = \beta = \begin{Bmatrix} \dot{p}_B + \tilde{\omega}_B p_B \\ \dot{\theta}_B \end{Bmatrix} = \begin{Bmatrix} v_B \\ \omega_B \end{Bmatrix} \quad (2.2)$$

$$\ddot{b} = \dot{\beta} = \begin{Bmatrix} \dot{v}_B + \tilde{\omega}_B v_B \\ \dot{\omega}_B \end{Bmatrix} = \begin{Bmatrix} \dot{v}_B \\ \dot{\omega}_B \end{Bmatrix} \quad (2.3)$$

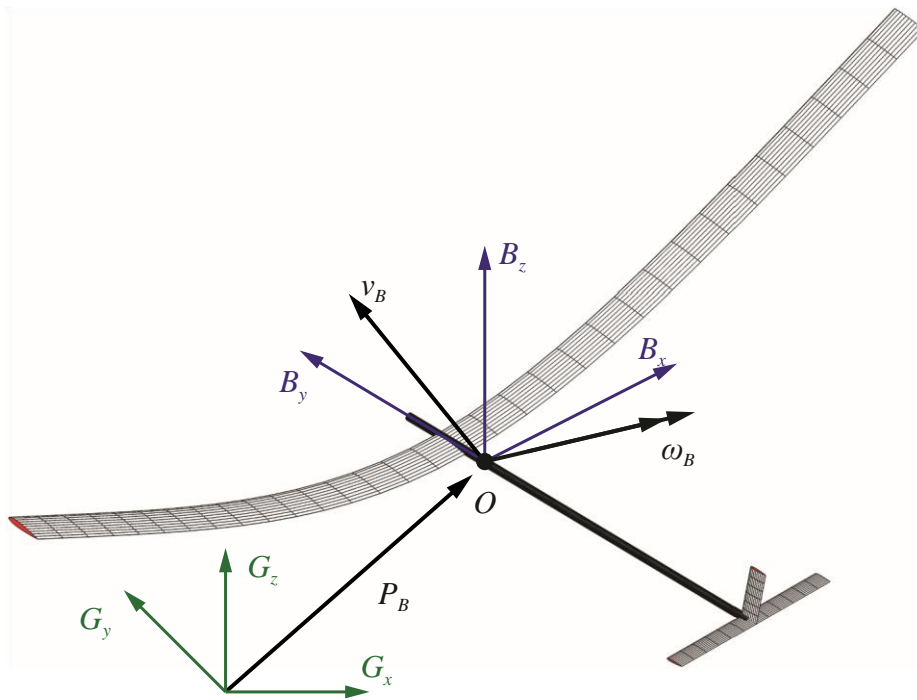


Figure 2.1 Body and global frame for rigid-body motion

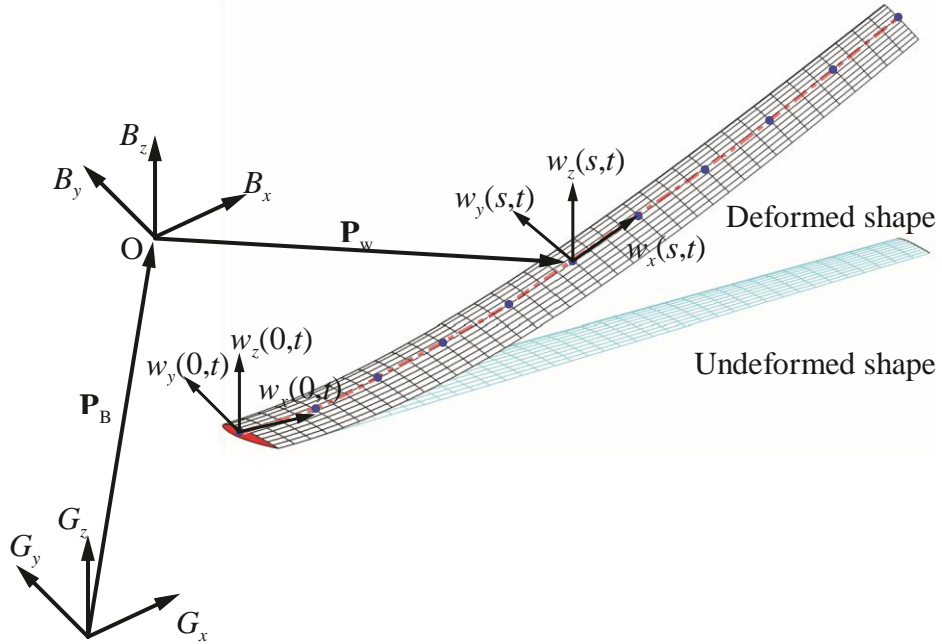


Figure 2.2 Flexible lifting-surfaces frames within the body frame

where p_B and θ_B are the body position and orientation of the aircraft resolved within the body frame. The $\tilde{\omega}_B$ is the skew-symmetric matrix of the angular velocity of the global frame rotating about the body frame. For a flexible wing, the nodal position and orientation of the flexible members are defined within a localized beam frame. This beam frame, w , is built within each wing element along the beam reference line in Figure 2.2. The beam frame is defined by $w_x(s,t)$ which points along the beam reference line, $w_y(s,t)$ which points towards the leading edge, and $w_z(s,t)$ which is the normal to the wing surface. The curvilinear coordinate, s , provides the nodal location within the body frame.

2.1.2 Elements with Constant Strain

Su and Cesnik [16] show that the elastic deformation of slender beams can be done with a nonlinear beam element. The strain and curvature of the beam reference line are considered the independent variables. The strain-based formulation allows simple shape functions to be defined for each element. Then, the strain vector of the element can be written as

$$\varepsilon_e^T = \{\varepsilon_x \quad \kappa_x \quad \kappa_y \quad \kappa_z\} \quad (2.4)$$

where ε_x is the extensional strain, κ_x is the twist, κ_y is the out-of-plane bending about the local w_y axis, and κ_z is the in-plane bending about the local w_z axis. The global strain vector for the aircraft is then created by combining each elemental strain vector from 1 to N.

$$\varepsilon^T = \{\varepsilon_1^T \quad \varepsilon_2^T \quad \dots \quad \varepsilon_N^T\} \quad (2.5)$$

where ε_N denotes the strain of the N th element. Complex nonlinear deformations can then be represented with this combination of elemental strain.

2.1.3 Equations of Motion

After defining the strain vector in Equation 2.4, the energy terms are resolved and Hamilton's principle is used to derive the equations of motions. Su and Cesnik [16] show the discretized equation of motion results as

$$\begin{aligned}
& \mathbf{M}_{FF}(\varepsilon)\ddot{\varepsilon} + \mathbf{M}_{FB}(\varepsilon)\dot{\beta} + \mathbf{C}_{FF}(\dot{\varepsilon}, \varepsilon, \beta)\dot{\varepsilon} + \mathbf{C}_{FB}(\dot{\varepsilon}, \varepsilon, \beta)\dot{\beta} + \mathbf{K}_{FF}\varepsilon \\
& = \mathbf{R}_F(\ddot{\varepsilon}, \dot{\varepsilon}, \varepsilon, \dot{\beta}, \beta, \lambda, \zeta, \mathbf{T}, \mathbf{u})
\end{aligned} \tag{2.6}$$

$$\begin{aligned}
& \mathbf{M}_{BF}(\varepsilon)\ddot{\varepsilon} + \mathbf{M}_{BB}(\varepsilon)\dot{\beta} + \mathbf{C}_{BF}(\dot{\varepsilon}, \varepsilon, \beta)\dot{\varepsilon} + \mathbf{C}_{BB}(\dot{\varepsilon}, \varepsilon, \beta)\dot{\beta} \\
& = \mathbf{R}_B(\ddot{\varepsilon}, \dot{\varepsilon}, \varepsilon, \dot{\beta}, \beta, \lambda, \zeta, \mathbf{T}, \mathbf{u})
\end{aligned} \tag{2.7}$$

The generalized force vector is

$$\begin{aligned}
\begin{Bmatrix} R_F \\ R_B \end{Bmatrix} &= \begin{Bmatrix} K_{FF}\varepsilon^0 \\ 0 \end{Bmatrix} + \begin{bmatrix} J_{p\varepsilon}^T \\ J_{pb}^T \end{bmatrix} B^F F^a + \begin{bmatrix} J_{p\varepsilon}^T \\ J_{\theta b}^T \end{bmatrix} B^M M^a + \begin{bmatrix} J_{h\varepsilon}^T \\ J_{hb}^T \end{bmatrix} N^g g + \begin{bmatrix} J_{p\varepsilon}^T \\ J_{pb}^T \end{bmatrix} T \\
& + \begin{bmatrix} \bar{B}_F \\ \bar{B}_B \end{bmatrix} u
\end{aligned} \tag{2.8}$$

The first term is pre-strain within the aircraft, the second term is the aerodynamic forces, the third term is the aerodynamic moments, the fourth term is the gravity force, the fifth term is the thrust force, and the last term is the required control force to maintain a certain wing shape. The rigid body equations are also defined as

$$\dot{\zeta} = -\frac{1}{2}\Omega_\zeta(\beta)\zeta \tag{2.9}$$

$$\dot{P}_B = [C^{GB}(\zeta) \ 0] \tag{2.10}$$

where b_c is the semi-chord, and d is the distance of the mid-chord in front of the reference axis. The quantity $-\frac{\dot{z}}{y}$ is the angle of attack that has contribution from the pitching angle and the unsteady plunging motion of the airfoil. Only the induced drag is taken into consideration as seen from the velocity components of figure 2.3. The inflow parameter λ_0 accounts for induced flow due to free vorticity, which is the summation of the inflow states λ as described in [Peters-Finite State] and given by

$$\dot{\lambda} = F_1 \begin{Bmatrix} \ddot{\epsilon} \\ \dot{\beta} \end{Bmatrix} + F_2 \begin{Bmatrix} \dot{\epsilon} \\ \beta \end{Bmatrix} + F_3 \lambda. \quad (2.14)$$

2.1.5 Controller Design

Using the non-linear equations of motion (equations 2.6, 2.7, 2.9, 2.10, 2.14), a complete linearization of the equations of motions [10] can be found. Assuming free flight only, the only loads applied to the system are from aerodynamics and gravity. Once linearized, each term can be grouped and finally written as equation 2.15

$$\begin{bmatrix} \dot{\epsilon} & \ddot{\epsilon} & \dot{\beta} & \dot{\zeta} & \dot{P}_B & \dot{\lambda} \end{bmatrix}^T = Q_1^{-1} Q_2 [\epsilon \quad \dot{\epsilon} \quad \beta \quad \zeta \quad P_B \quad \lambda]^T + Q_1^{-1} Q_3 [\delta_e]^T, \quad (2.15)$$

Which can be otherwise written as

$$\dot{x} = Ax + Bu \quad (2.16)$$

where the state vector is

$$x = [\varepsilon \quad \dot{\varepsilon} \quad \beta \quad \zeta \quad P_B \quad \lambda]^T \quad (2.17)$$

and the coefficients of each state represented in matrix form can be rewritten as

$$Q_1 = \begin{bmatrix} I & 0 & 0 & 0 & 0 & 0 \\ 0 & \bar{M}_{FF} & \bar{M}_{FB} & 0 & 0 & 0 \\ 0 & \bar{M}_{FF} & \bar{M}_{FB} & 0 & 0 & 0 \\ 0 & 0 & 0 & I & 0 & 0 \\ 0 & 0 & 0 & 0 & I & 0 \\ 0 & -F_{1F} & -F_{1B} & 0 & 0 & I \end{bmatrix} \quad (2.18)$$

$$Q_2 = \begin{bmatrix} 0 & I & 0 & 0 & 0 & 0 \\ -\bar{K}_{FF} & -\bar{C}_{FF} & -\bar{C}_{FB} & \frac{R_F^{grav}}{\bar{\zeta}_0} & 0 & \frac{R_F^{aero}}{\lambda_0} \\ 0 & -\bar{C}_{BF} & -\bar{C}_{BB} & \frac{R_B^{grav}}{\bar{\zeta}_0} & 0 & \frac{R_B^{aero}}{\lambda_0} \\ 0 & 0 & -\frac{1}{2} \Omega_\zeta \frac{\zeta_0}{\beta_0} & -\frac{1}{2} \Omega_\zeta & 0 & 0 \\ 0 & 0 & [C^{GB} \quad 0] & [C_{/\zeta_0}^{GB}] \beta_0 & 0 & 0 \\ 0 & F_{2F} & F_{2B} & 0 & 0 & F_3 \end{bmatrix} \quad (2.19)$$

$$Q_3 = \begin{bmatrix} J_{p\varepsilon}^T \\ J_{pb}^T \end{bmatrix} \quad (2.20)$$

$$A = Q_1^{-1}Q_2 \tag{2.21}$$

$$B = Q_1^{-1}Q_3 . \tag{2.22}$$

Once the linearized equations of motion are converted to state space form, the aircraft is then trimmed [7] for steady level flight using body angle, thrust, and elevator inputs. This trim state will be used as the goal of the controller, as it pushes the strain and strain rates back to their trimmed states through the use of the aircraft's elevators. Then the following feedback loop Figure 2.5 can be defined.

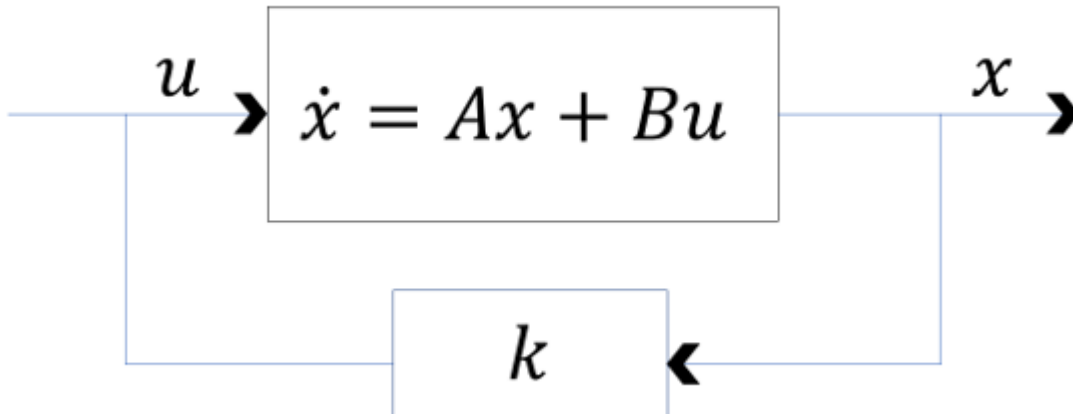


Figure 2.4 Block diagram of control scheme

MATLAB's linear-quadratic regulator (LQR) design is used to determine k . The state-feedback law $u = -kx$ is used to minimize the quadratic cost function

$$J(u) = \int_0^{\infty} (x^T Q x + u^T R u + 2x^T N u) dt \tag{2.23}$$

and k is found by

$$k = R^{-1}(B^T S + N^T) \quad (2.24)$$

where Q and R are weighting functions for state and input matrices, respectively. S is the solution of the Riccati equation

$$A^T S + SA - (SB + N)R^{-1}(B^T S + N^T) + Q = 0 \quad (2.25)$$

This paper does not consider the cross-term matrix N . Only the strain and strain rate states are used in the above feedback loop, specifically

$$x = [\varepsilon \ \dot{\varepsilon}]^T . \quad (2.26)$$

The rigid body motion state β was included in certain cases but was found to not have a beneficial impact on the aircraft's performance and thus not considered further. In order to implement the controller in the time domain, the control input is more accurately represented as

$$u_i = u_o - \Delta u \quad (2.27)$$

where

$$\Delta u = -k\Delta x \quad (2.28)$$

and

$$\Delta x = \begin{Bmatrix} \varepsilon_i - \varepsilon_o \\ \dot{\varepsilon}_i - \dot{\varepsilon}_o \end{Bmatrix} \quad (2.29)$$

The i^{th} terms are the current time step, and the o^{th} terms are the initial trimmed states. It should be noted that the weighting matrices Q and R were not optimized in any way and trial-and-error was used for iterating the weights. For selecting initial values of Q and R , Bryson's rule was loosely followed:

$$Q_{ii} = \frac{1}{\text{maximum acceptable value of } x_i^2} \quad (2.30)$$

$$R_{jj} = \frac{1}{\text{maximum acceptable value of } u_j^2} \quad (2.31)$$

where i and j are incremented for every state and control input, respectively. This essentially scales the variables so that the maximum allowed value is 1 for each term.

2.1.6 Aircraft Model

The aircraft model in Figure 2.5 is similar in geometry to the model used by Su and Cesnik [10] but with a larger flat bending rigidity in the wings. The complete list of the aircraft's mass, stiffness, and inertia properties can be found in previous work [10]. The aircraft is trimmed at an altitude of 6096 m (20,000 ft) for each flight speed: 90 m/s, 110 m/s and 120 m/s. A 125 m/s case will be examined to determine the robustness of the controller.

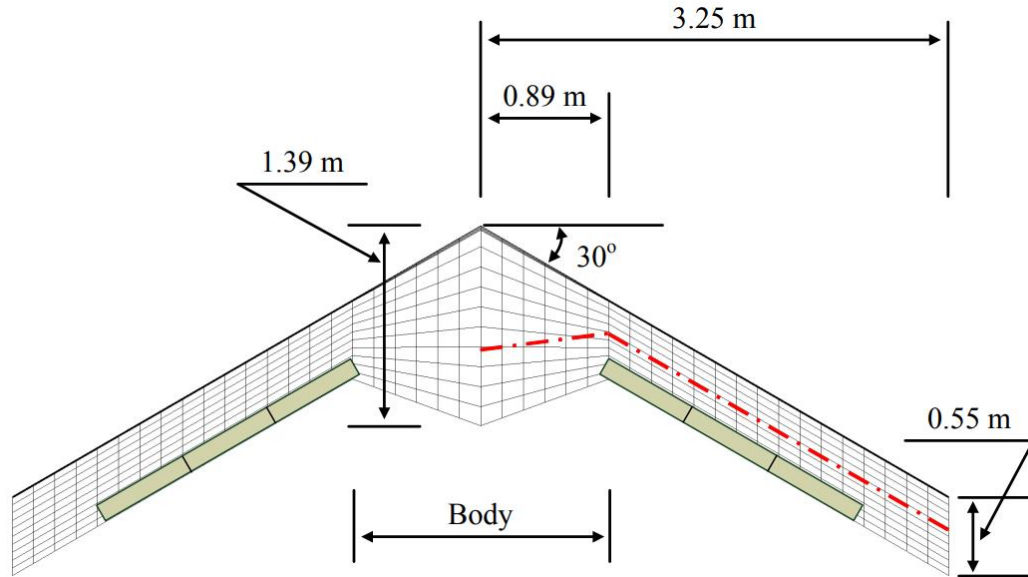


Figure 2.5 Geometry of Blended-Wing-Body aircraft

In Figure 2.6, the root locus of the BWB aircraft at incrementing speeds from 100 m/s (triangle) to 125 m/s (square) is shown. The coupled bending modes are stable initially but transition to unstable at 112 m/s. Therefore, a pre- and post- flutter flight speed is needed to examine how the controller handles the instability. Figure 2.7 shows that the phugoid and short period modes are stable throughout the entire range.

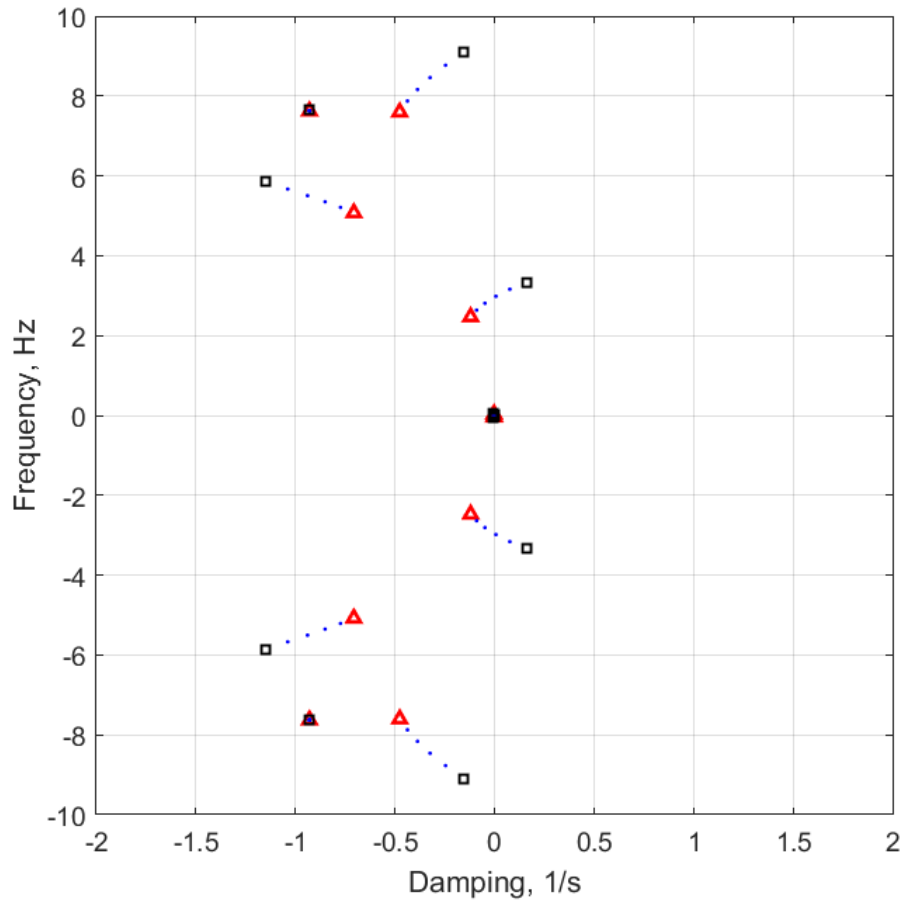


Figure 2.6 Root locus plot with increasing velocities

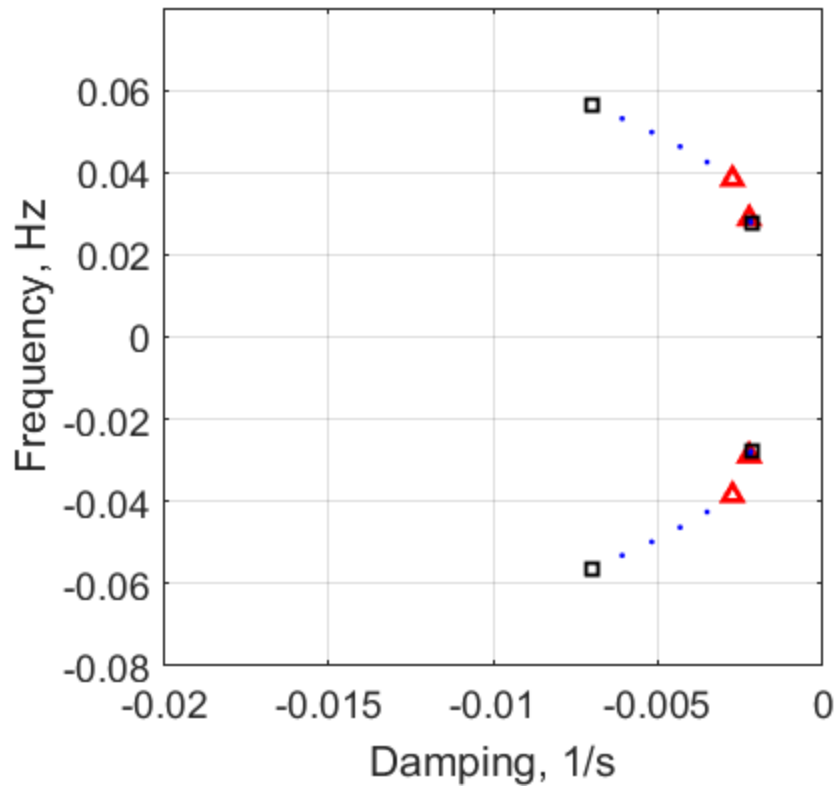


Figure 2.7 Zoomed in root locus plot

2.1.7 Gust Model

With the aircraft model defined and stability boundary determined, it is now necessary to define the models that will be used to excite the aircraft. Two gust models will be used to examine the aeroelastic response and flight dynamics of the aircraft: a discrete (1-cosine) and a continuous Dryden gust. The discrete gust model used has a spatial distribution governed by a 1-cosine function

$$w_g = \frac{w_o}{2} \left(1 - \cos \frac{2\pi x}{25c}\right) \quad (2.32)$$

For this case, the gust has a maximum radius of 25 meters and a maximum gust speed center amplitude, w_o , of 3.6 m/s. The gust strength at each time step is assumed to be constant along the entire wing, that is each element sees the same portion of the gust. The gust is offset by 18 meters, giving the aircraft a short amount of time to fly unperturbed before experiencing the gust.

The continuous gust model used is a Dryden gust model. The Dryden model uses a power spectral density (PSD) function to describe atmosphere turbulence. The PSD is

$$\Phi_w(\omega) = \frac{\sigma_w^2 L_w \left[1 + 3\left(\frac{L_w \omega}{U_\infty}\right)^2\right]}{\pi U_o \left[1 + 3\left(\frac{L_w \omega}{U_\infty}\right)^2\right]^2} \quad (2.33)$$

where L_w is the scale of turbulence, determined by the aircraft altitude [8]. The root mean square vertical gust velocity, σ_w , is 6 m/s which at 6096 m of altitude is classified as moderate gust [13]. The aircraft trim velocity is U_∞ .

3 DYNAMIC RESPONSE

The open loop and closed loop flight dynamics of the BWB will be compared. For the discrete and continuous gust, different flight speeds will be considered. How the aircraft responds to different perturbation frequencies and magnitudes will be examined as well as how well the controller is able to reduce these dynamic responses.

3.1 Discrete Gust (1-cosine)

The first step is to examine the baseline flight dynamics of the model. The nominal flight speed will be used to determine how the model responds to the discrete gust case.

3.1.1 90 m/s

The open loop performance of the BWB at 90 m/s with the discrete gust applied is a baseline for the other flight profiles. The aircraft begins to fly through the gust after a few tenths of a second and is excited by the gust. Although the open loop response is stable, the goal of the controller is to reduce the frequency of the vibration and reduce the magnitude of the strains. In Figure 3.1, the open loop response experiences seven periods of vibration with amplitude of over two degrees in the first four seconds. Applying the LQR controller reduces the period count to three with an amplitude of less than one degree. The frequency of vibration is reduced by half. The wing tip in Figure 3.2 also experiences less vibration and a reduced magnitude. The root bending moment of the wing in Figure 3.3 is reduced by

100 newton meters. This is accomplished with a max outer elevator deflection of four degrees in Figure 3.4. However, the elevator experiences a control input of -4 to 4 degrees within a tenth of a second.

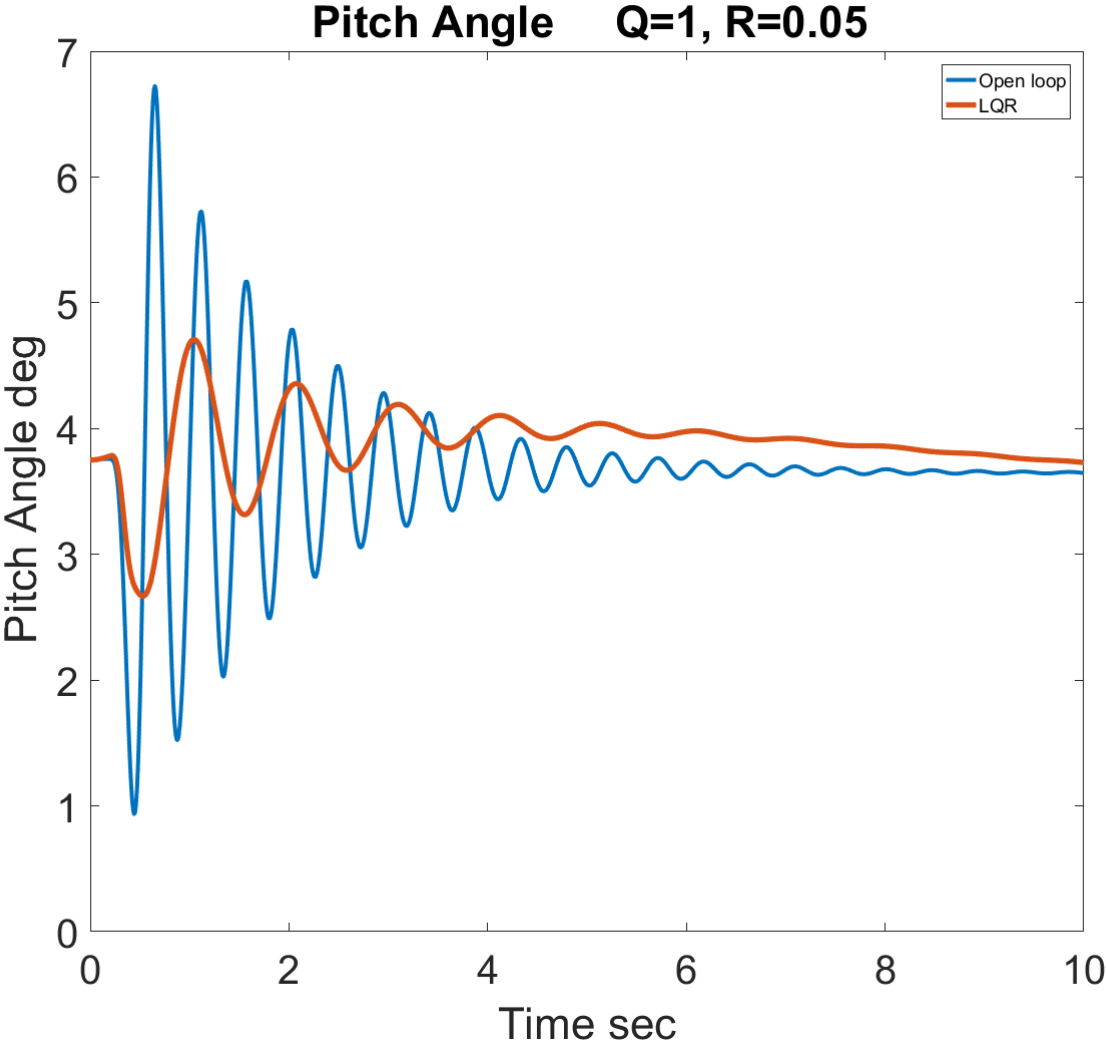


Figure 3.1 Pitch Angle for discrete gust at 90m/s

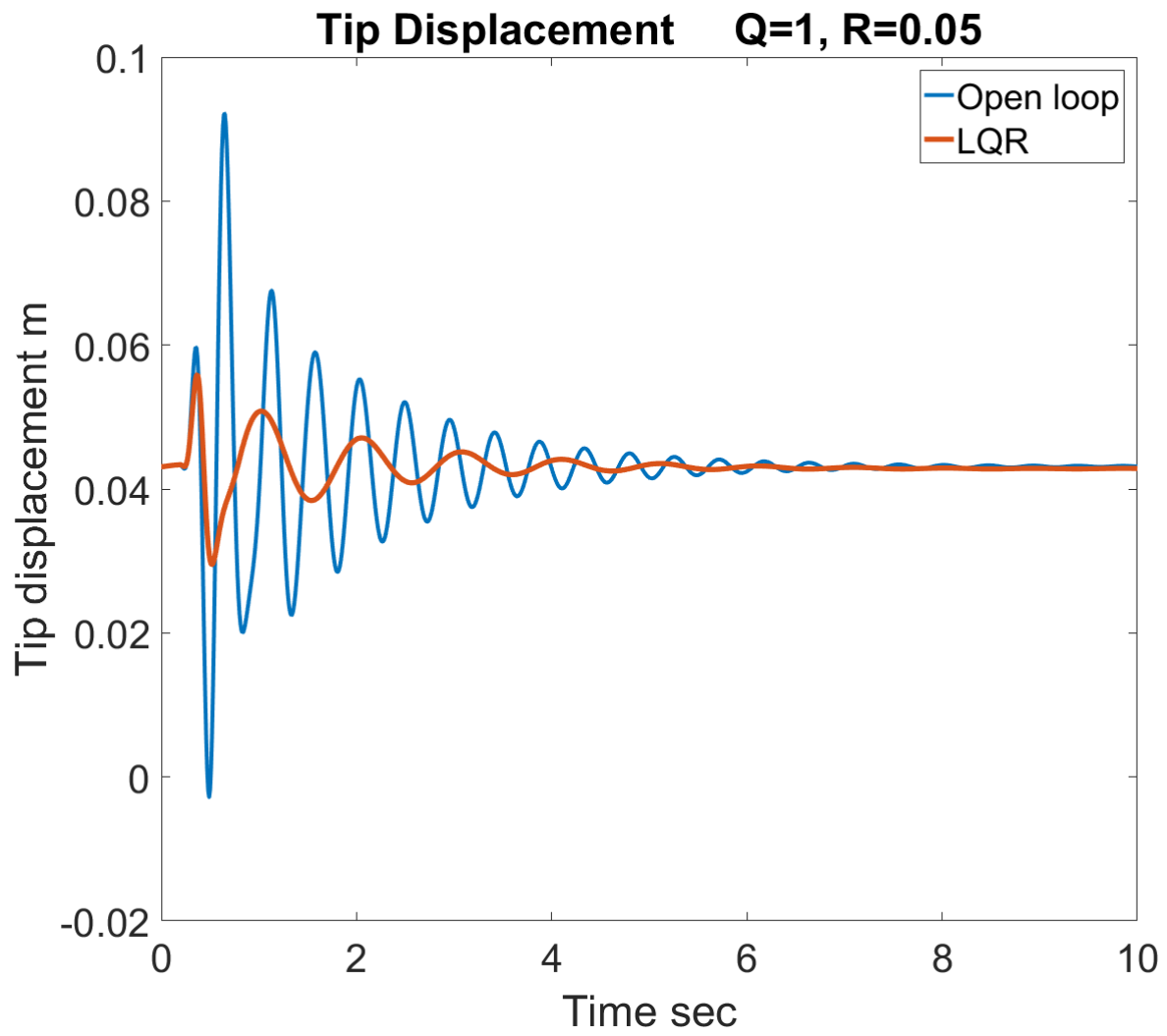


Figure 3.2 Tip displacement for discrete gust at 90m/s

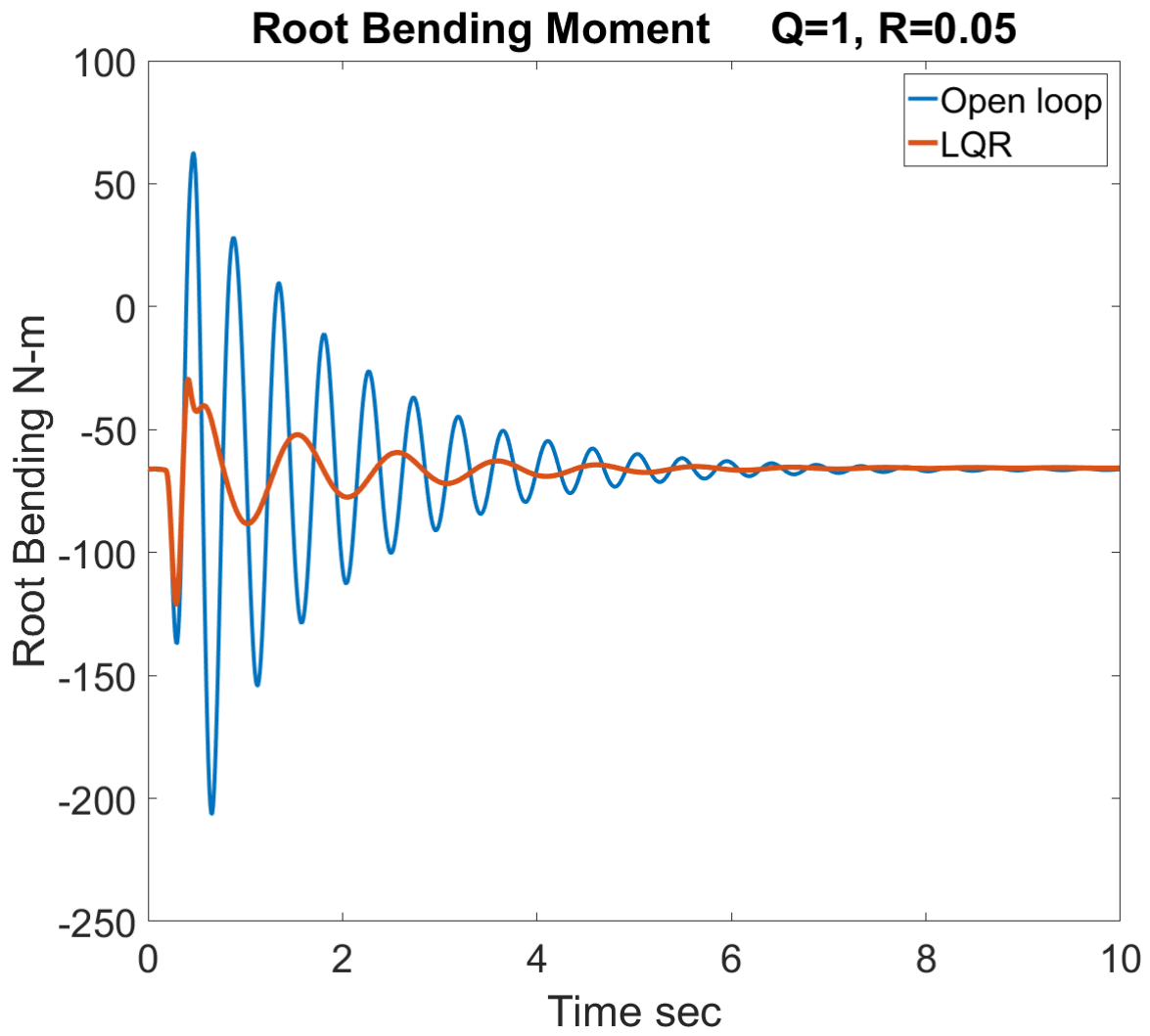


Figure 3.3 Root bending moment for discrete gust at 90m/s

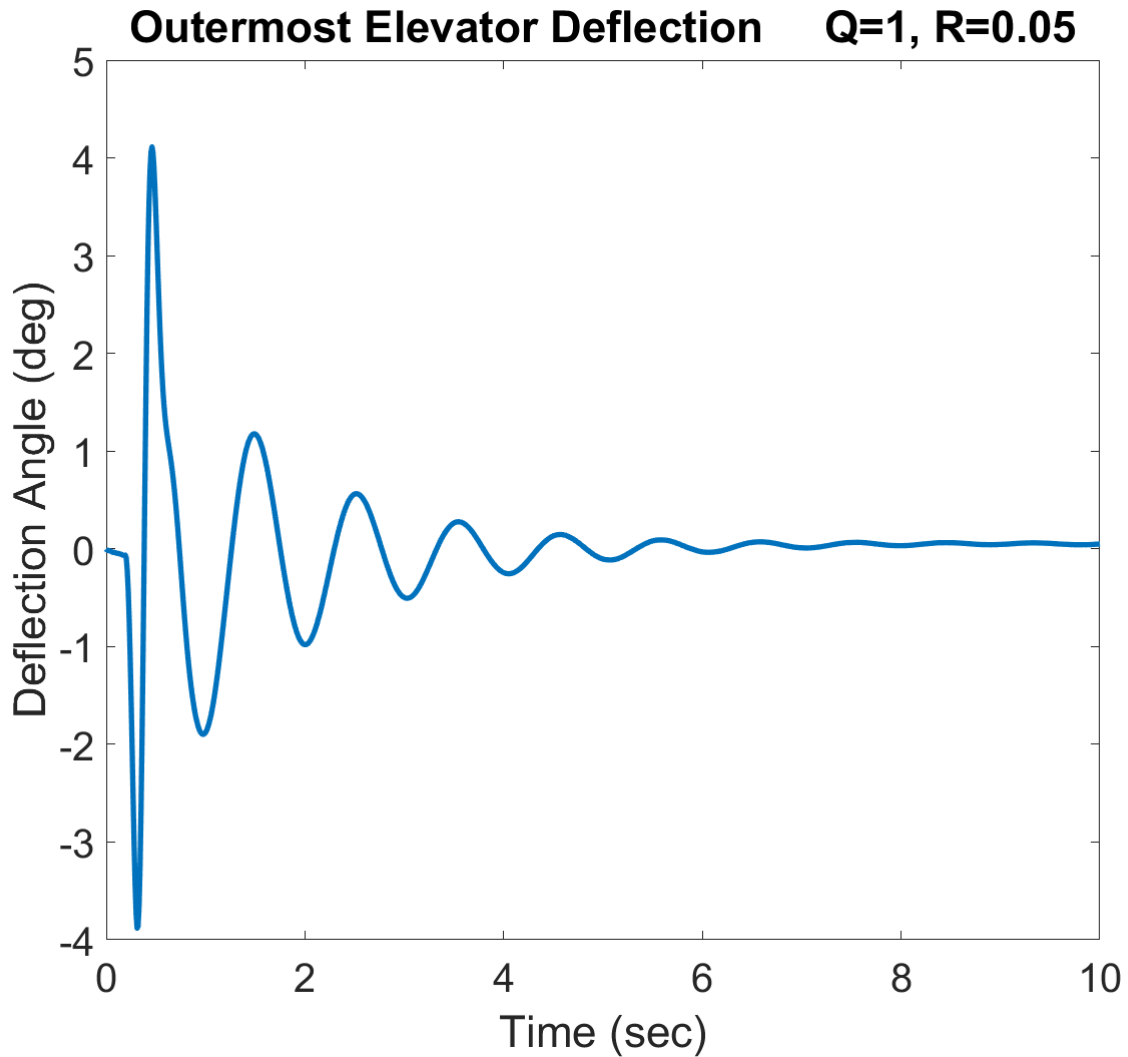


Figure 3.4 Outer elevator deflection for discrete gust at 90m/s

3.1.2 110 m/s

The pre-flutter speed at 110 m/s shows an increase in the frequency of vibration in the pitch of Figure 3.5 as well as an increased loading on the wings, as indicated by the root bending moment in Figure 3.7. The controller performs similarly at a higher speed, reducing the number of periods in the first four seconds of the pitch angle from 11 to 5. Although the tip displacement and root bending moment have their frequency and

magnitudes reduced, similar to the 90 m/s case, both cases suffer from the quick elevator deflection rate. Because the elevator Figure 3.8 experiences an 8-degree shift within a small amount of time, some sort of smoothing function or rate control would need to be implemented. Having such a sudden shift in elevator deflection may cause issues with the elevator actuator in an actual aircraft.

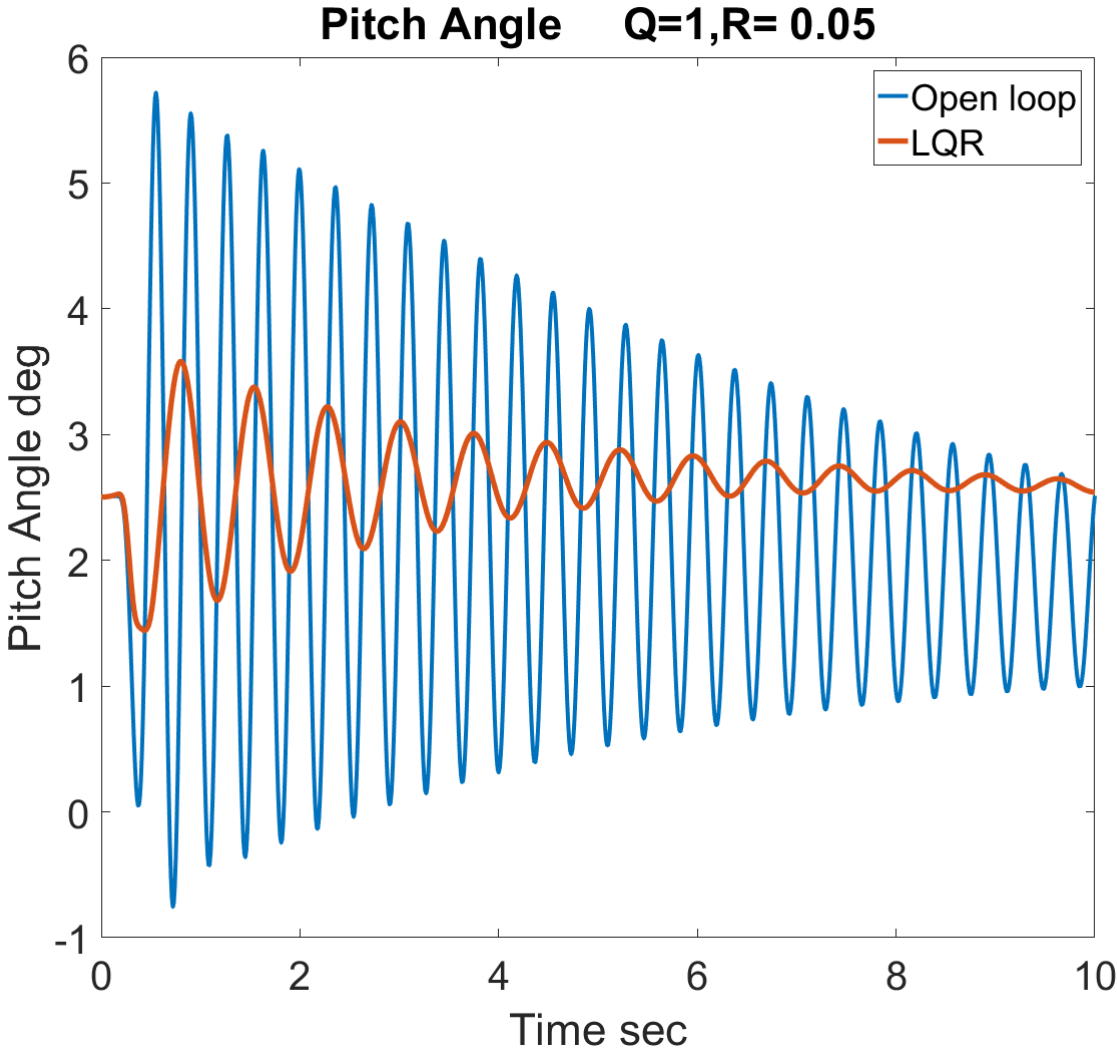


Figure 3.5 Pitch angle for discrete gust at 110m/s

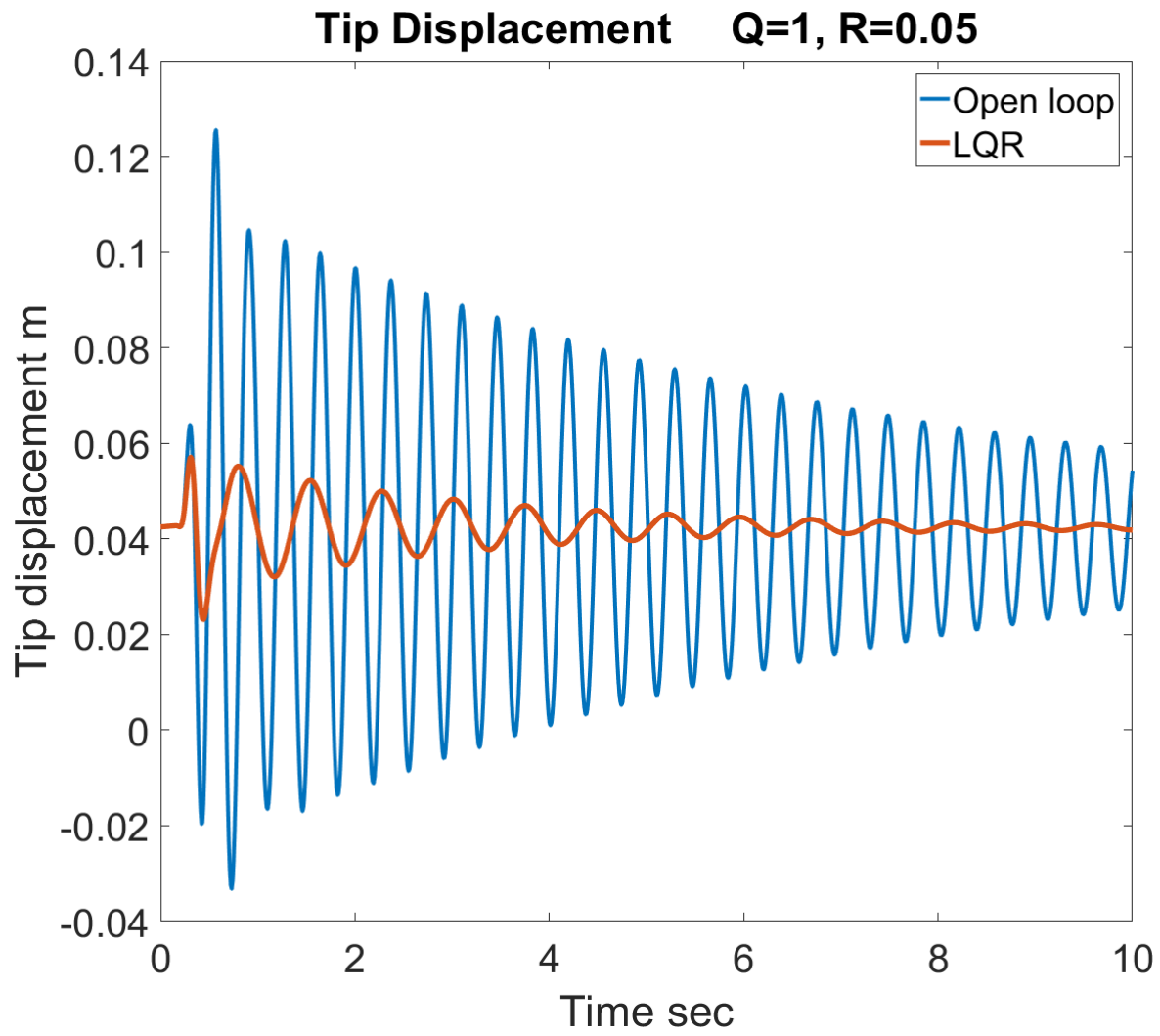


Figure 3.6 Tip displacement for discrete gust at 110m/s

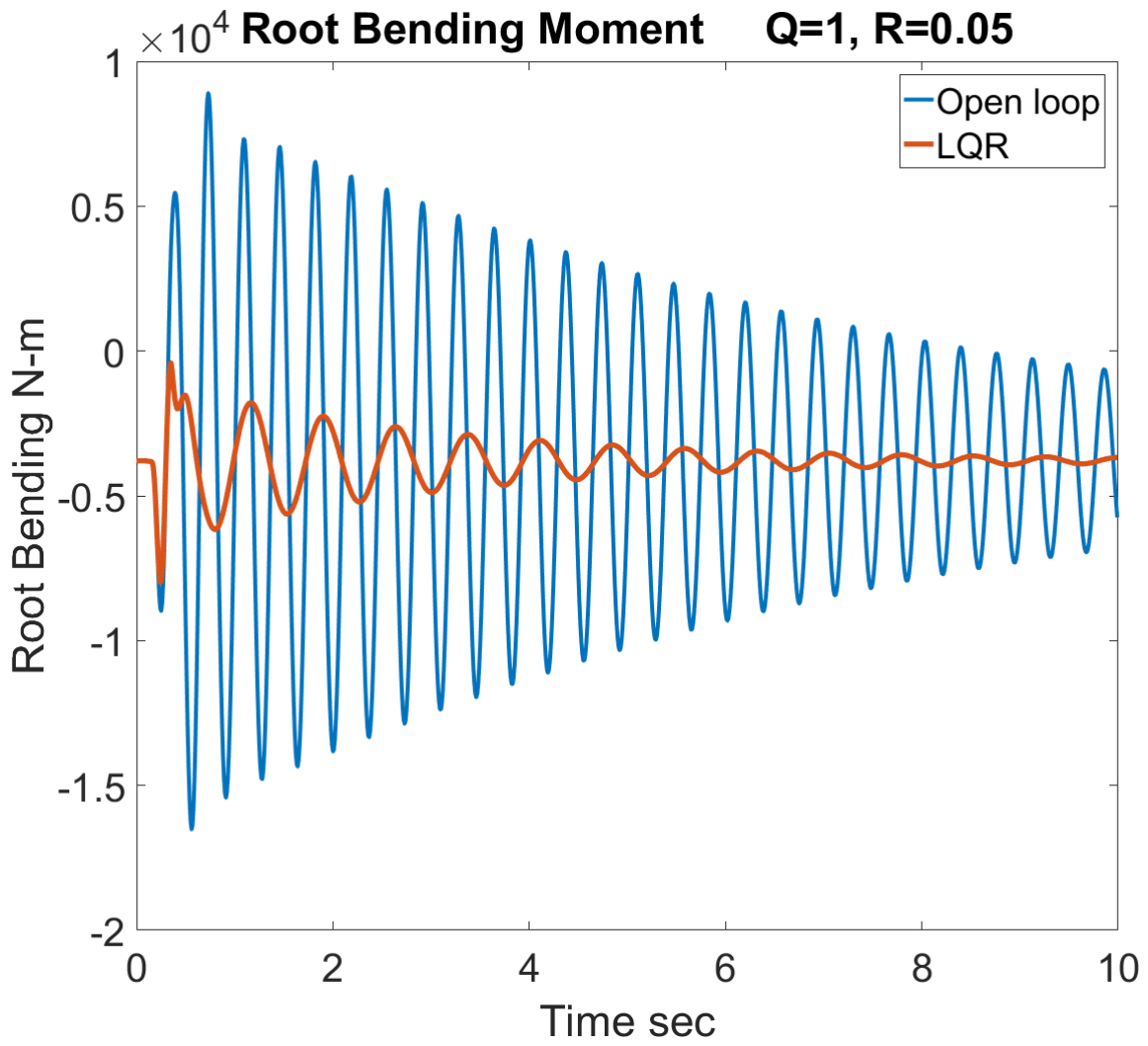


Figure 3.7 Root bending moment for discrete gust at 110m/s

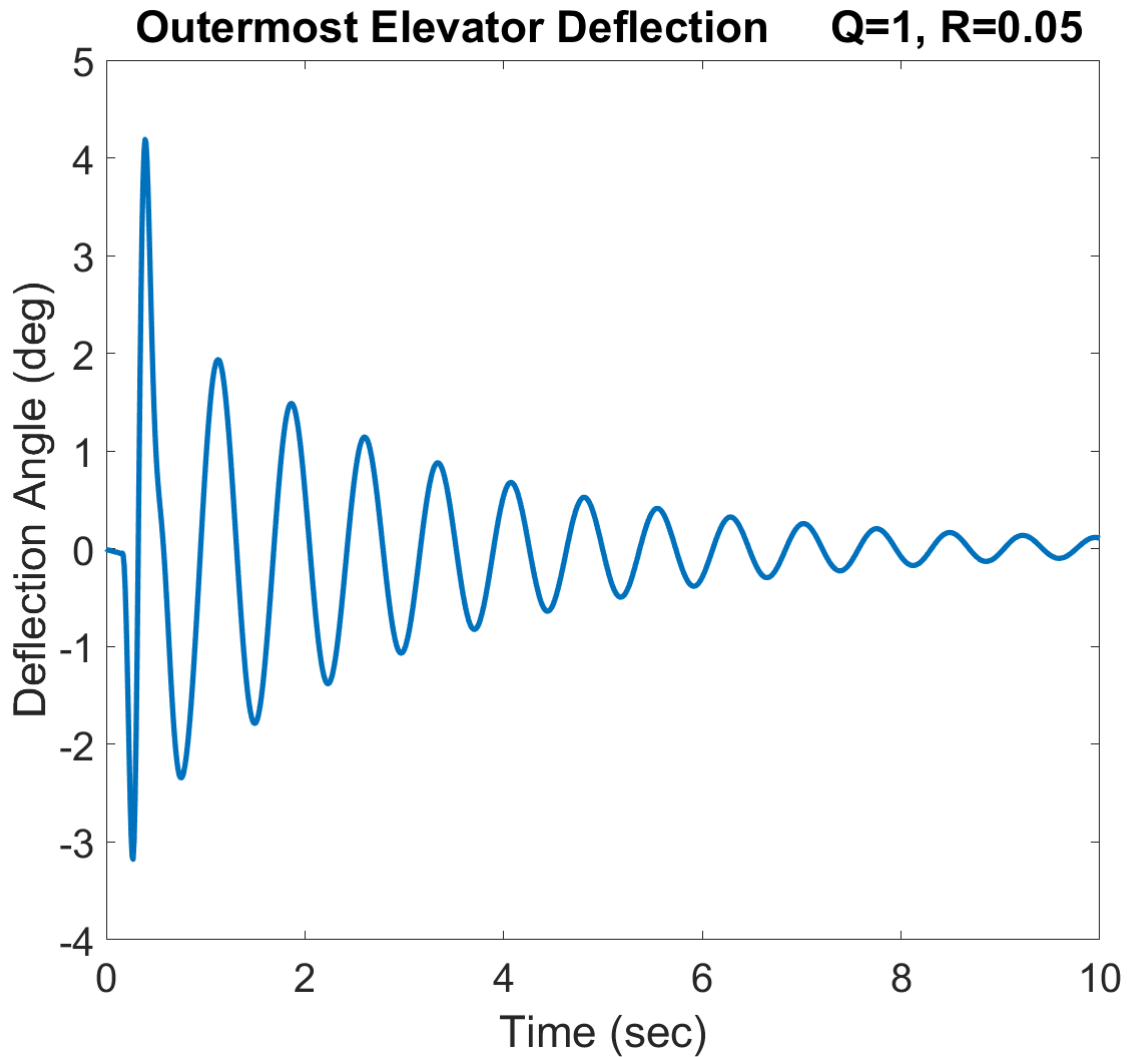


Figure 3.8 Outer elevator deflection for discrete gust at 110m/s

3.1.3 120 m/s

At 120 m/s, the aircraft is past its flutter boundary of 112 m/s and plunges as shown in Figure 3.9. In Figure 3.10, the pitch settles at -90 degrees and oscillates around it, nose down. While this is unrealistic, the aircraft becomes unflyable within 10 seconds. The controller is able to effectively control this instability as well as drastically improve the strain experienced by the aircraft as seen in Figure 3.12 where the root bending moment of

the aircraft is reduced by an order of magnitude. In Figure 3.11 the controller is able to reduce the tip vibration frequency. As seen in the previous cases, the elevator in Figure 3.13 only experiences an 8 degree shift again.

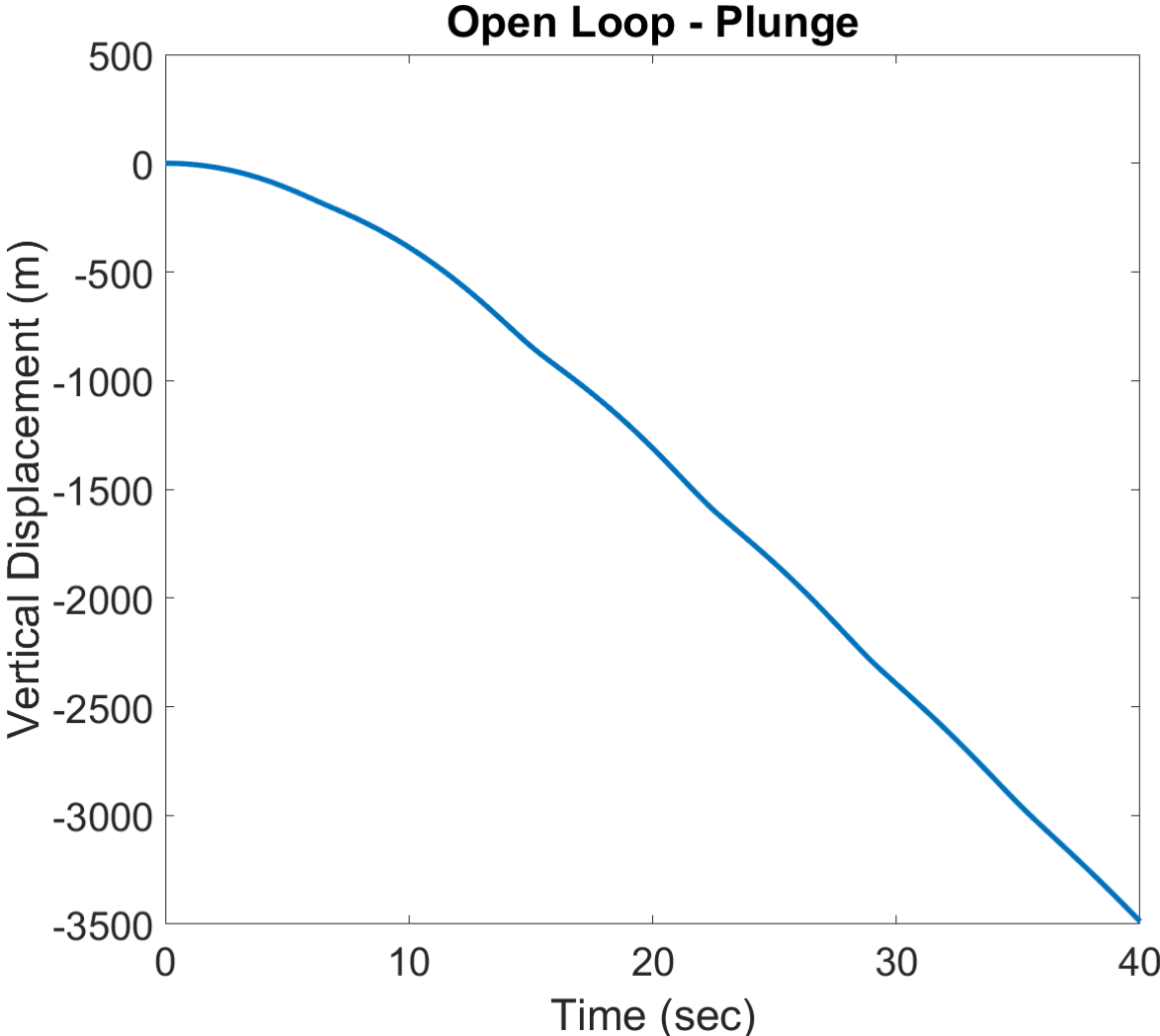


Figure 3.9 Plunge for discrete gust at 120m/s

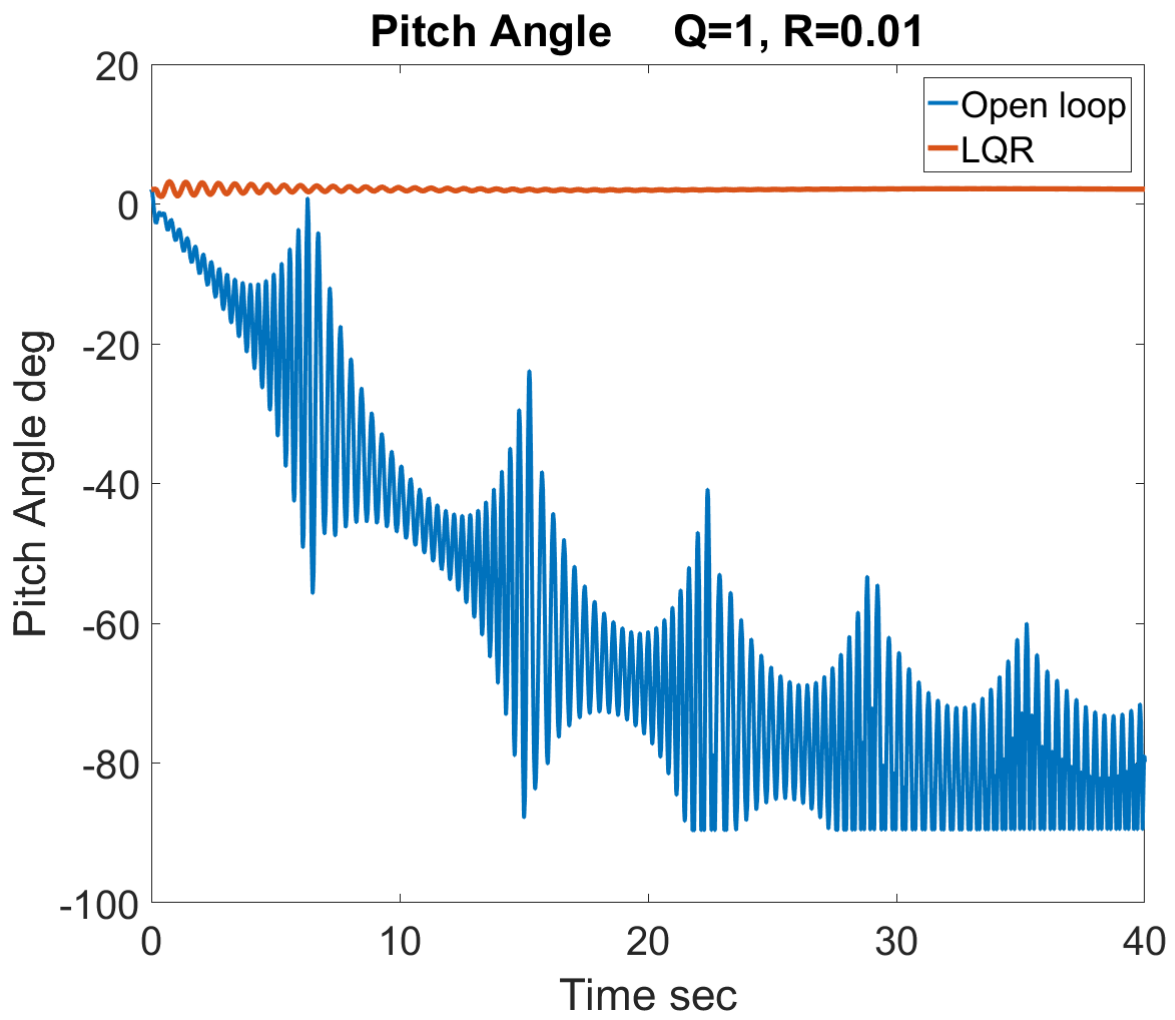


Figure 3.10 Pitch angle for discrete gust at 120m/s

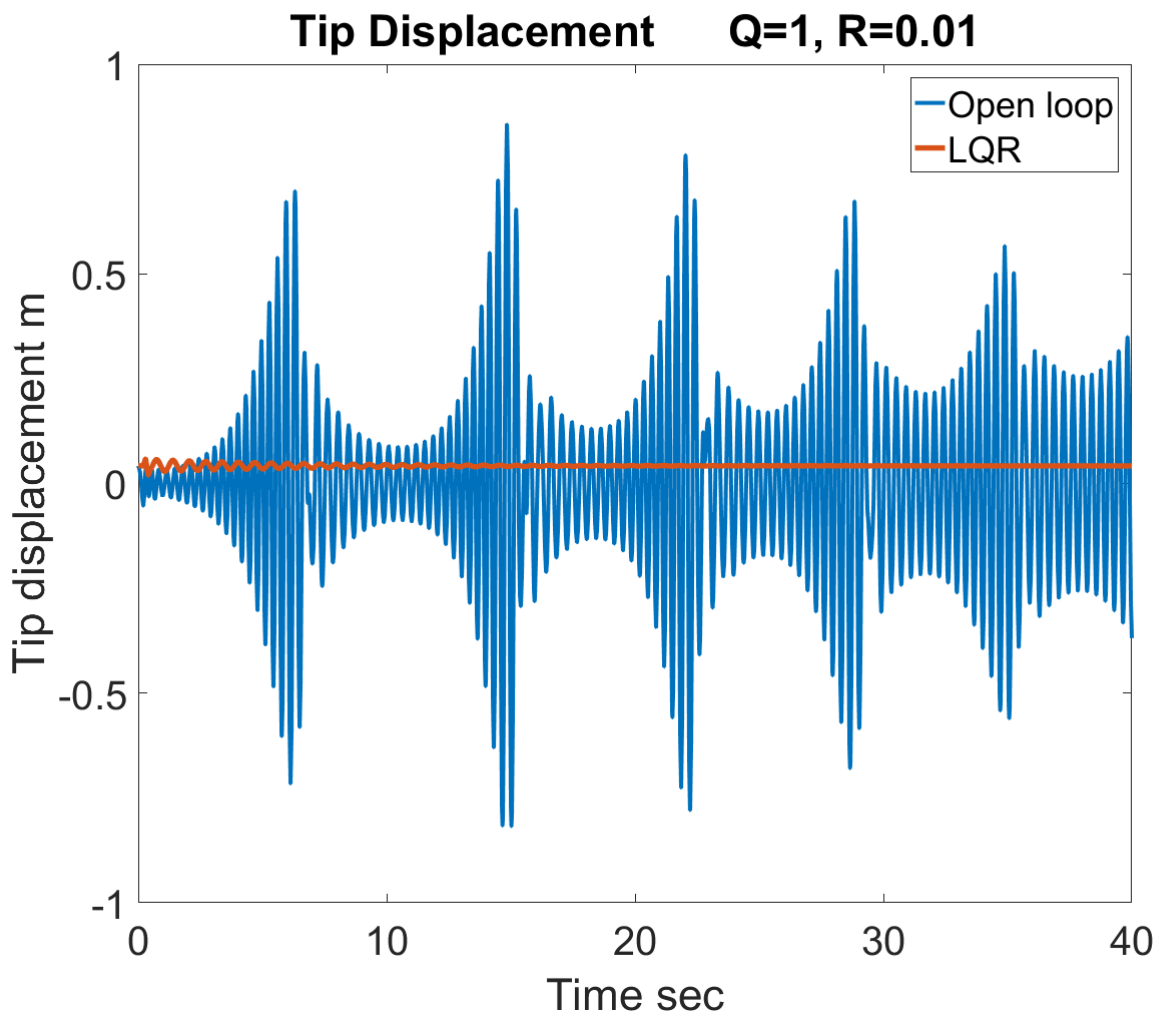


Figure 3.11 Tip displacement for discrete gust at 120 m/s

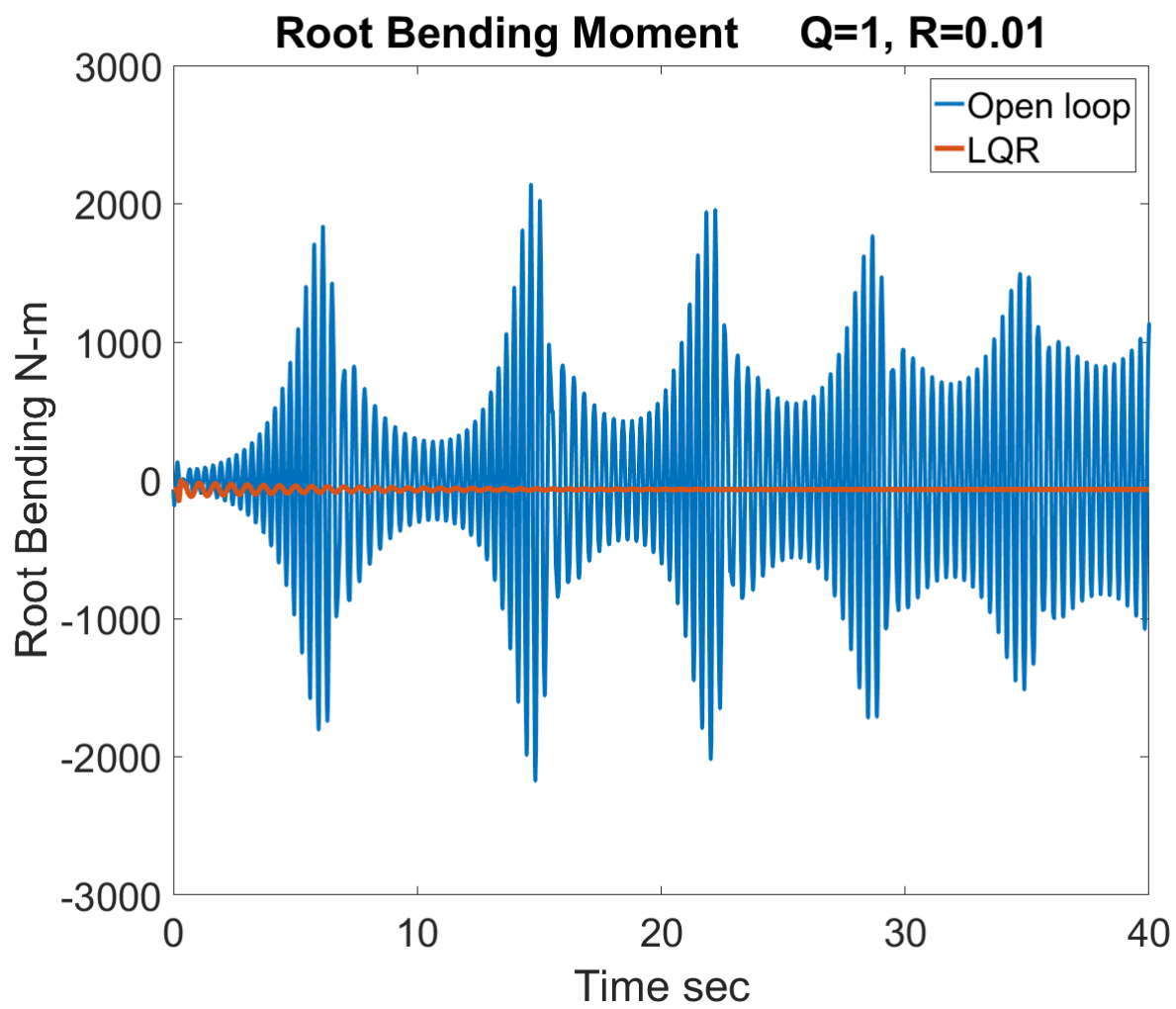


Figure 3.12 Root bending moment for discrete gust at 120m/s

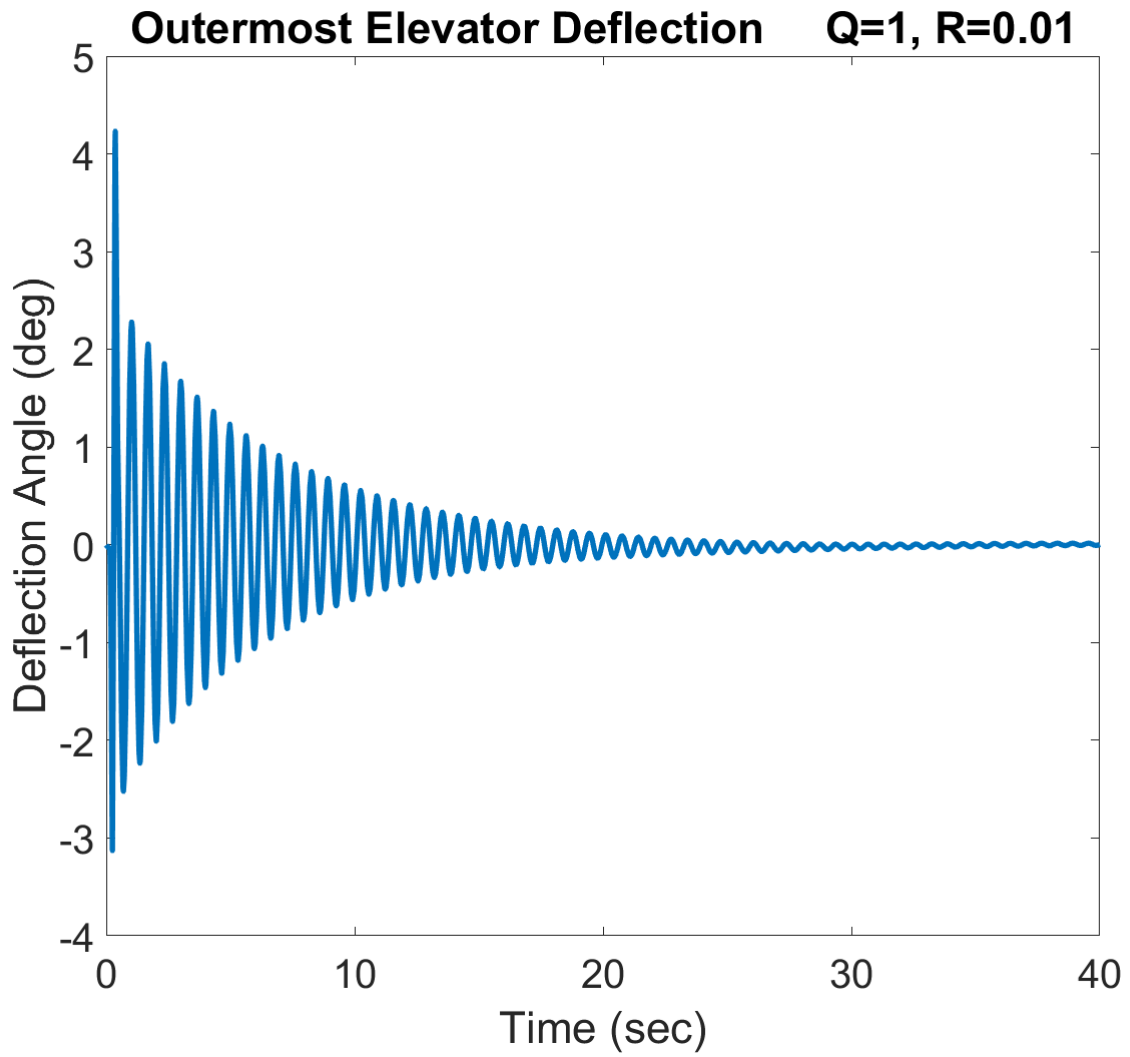


Figure 3.13 Outer elevator deflection for discrete gust at 120m/s

3.2 Continuous Gust - Dryden

The discrete gust acted similarly to an impulse function, where the aircraft is perturbed for a short amount of time then left to vibrate on its own. A continuous gust will provide a different challenge for the controller, where it does not give the aircraft time to settle and is continuously excited.

3.2.1 90 m/s

By the nature of the stochastic gust, the applied perturbation to the aircraft has an increased frequency. This will give less time for the aircraft to recover from a borderline unstable state. At 90 m/s the aircraft is still stable but the LQR controller is able to reduce the frequency and magnitude of the vibrations as seen in Figures 3.14, 3.15, and 3.16. Compared to the other cases, the weighting matrices Q for this case is much larger, 12 compared to 1. This could potentially be the reason the controller is unable to perform as well as it has in the discrete gust case. With a larger Q , the controller is allowing larger values for the states being controlled. This would explain why the minimum and maximum magnitudes of the open and closed response are closely aligned for the pitch angle. The tip displacement Figure 3.15 as well as root bending moment of Figure 3.16 are reduced but not as efficiently as the discrete gust cases. The elevator experiences a similar shifting pattern in Figure 3.17 as the previous cases. Higher speeds will need to be examined to see if the LQR controller can adequately alleviate the dynamic response to the stochastic gust.

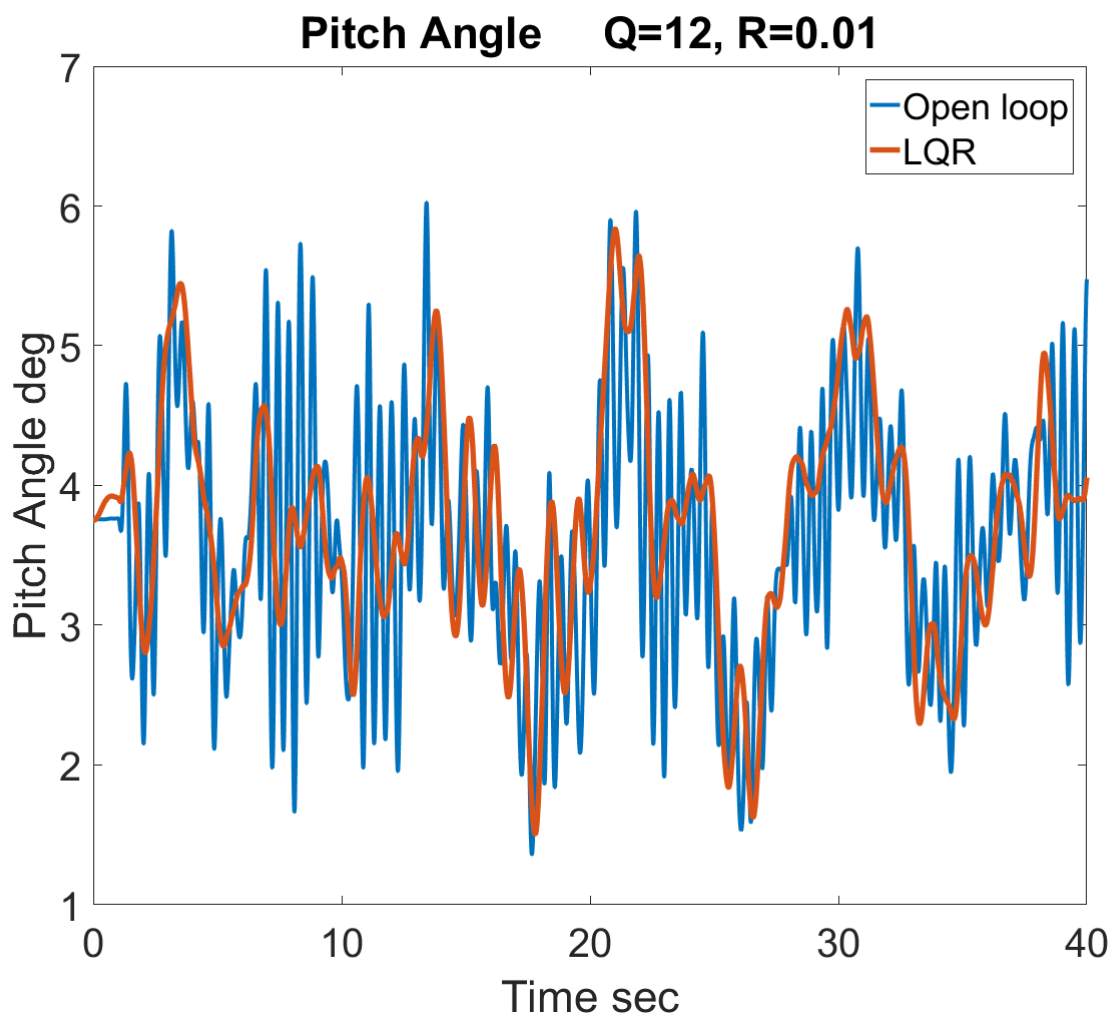


Figure 3.14 Pitch angle for continuous gust at 90m/s

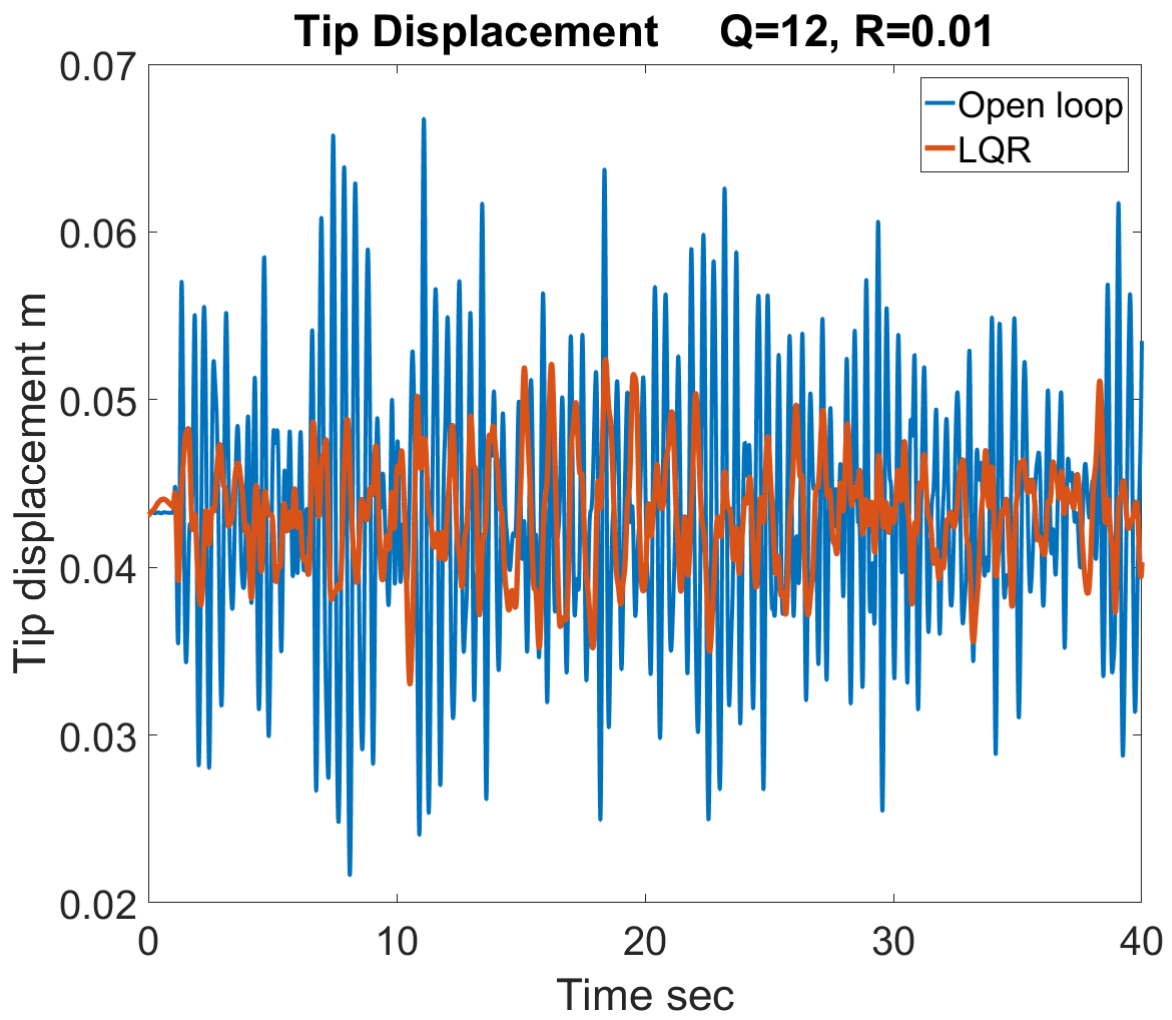


Figure 3.15 Tip displacement for continuous gust at 90m/s

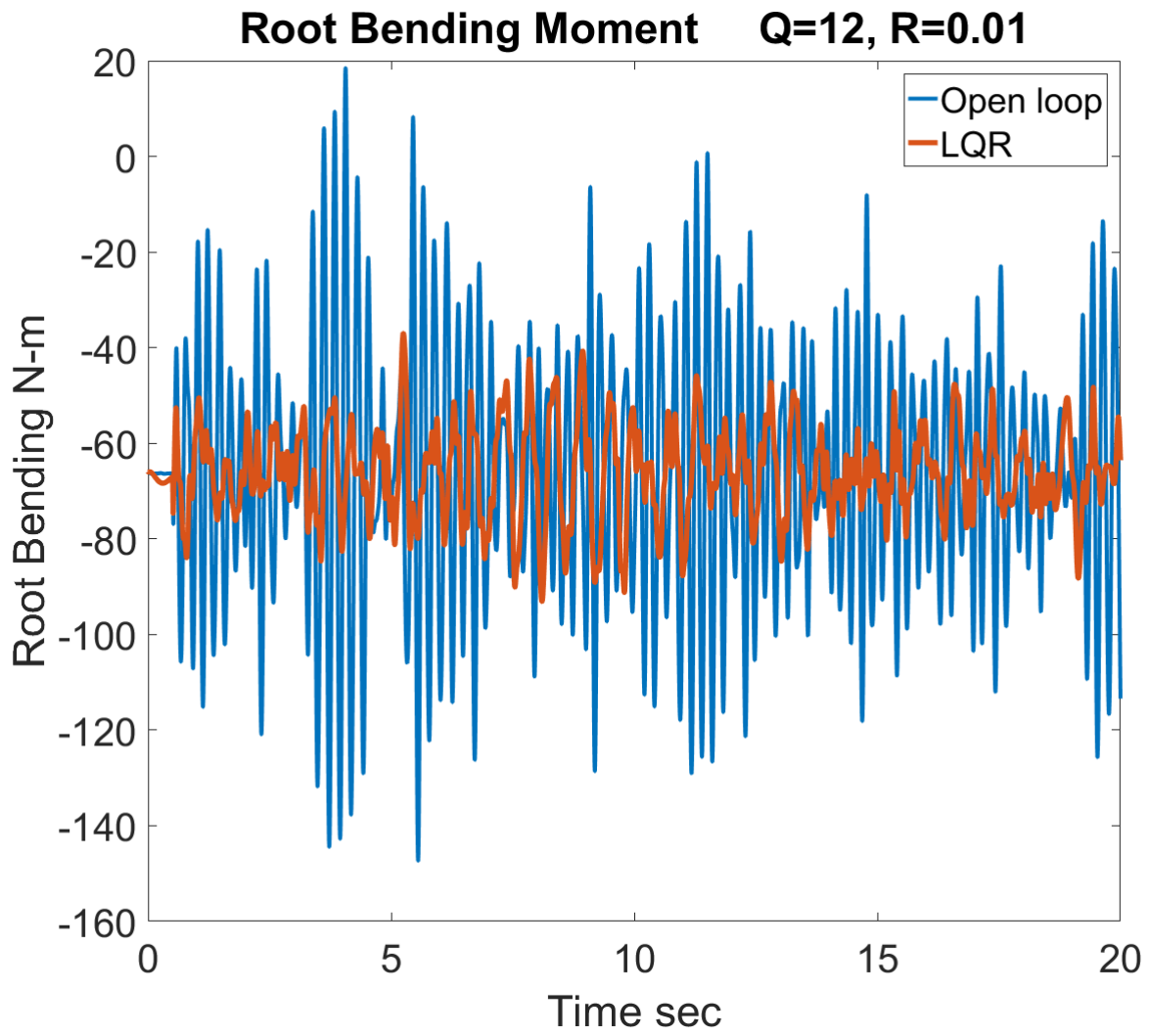


Figure 3.16 Root bending moment for continuous gust at 90m/s

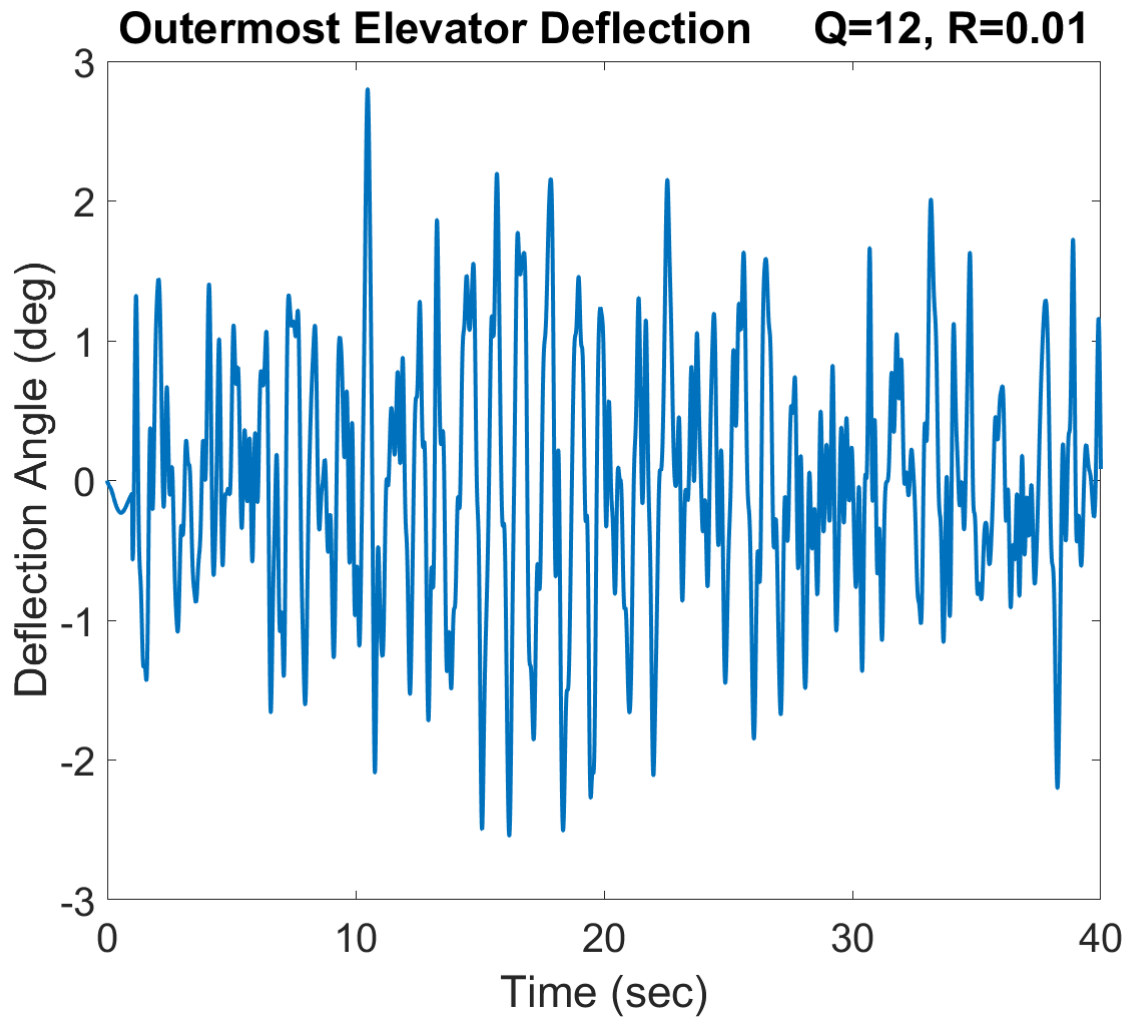


Figure 3.17 Outer elevator deflection for continuous gust at 90m/s

3.2.2 110 m/s

At 110 m/s and with the continuous gust applied, the aircraft experiences instability. As shown in Figure 3.18, the LQR controller is able to suppress this instability and regain control of the aircraft, but the pitch angle still has an increased frequency in Figure 3.19. The frequency of the oscillation is increased and appears to have its amplitude

growing in the open loop case. The controller is able to suppress this growth as well as reduce the amplitude of the tip displacement in Figure 3.20 and root bending moment in Figure 3.21. The elevator sudden shifting in Figure 3.22 is made worse in this case, with a quicker oscillation.

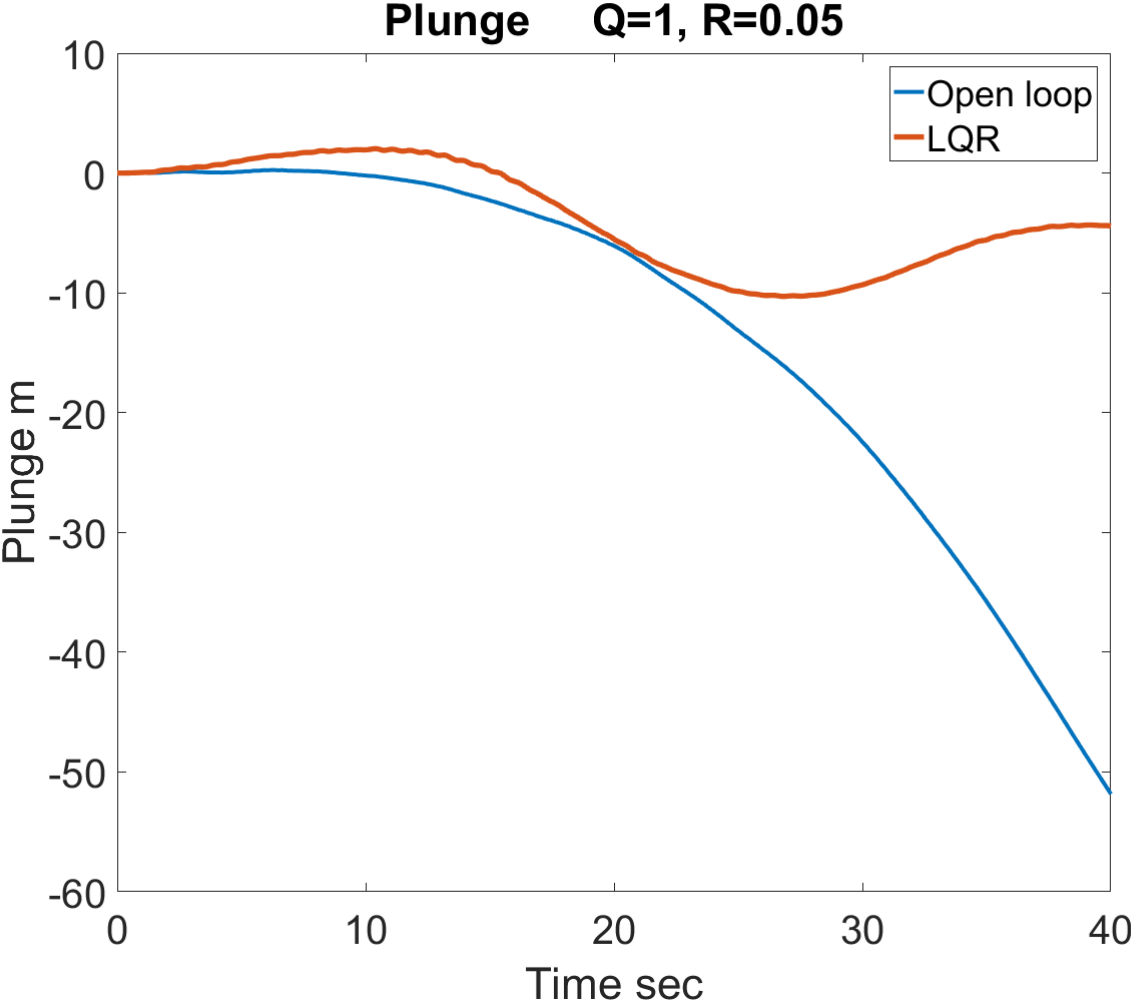


Figure 3.18 Plunge for continuous gust at 110m/s

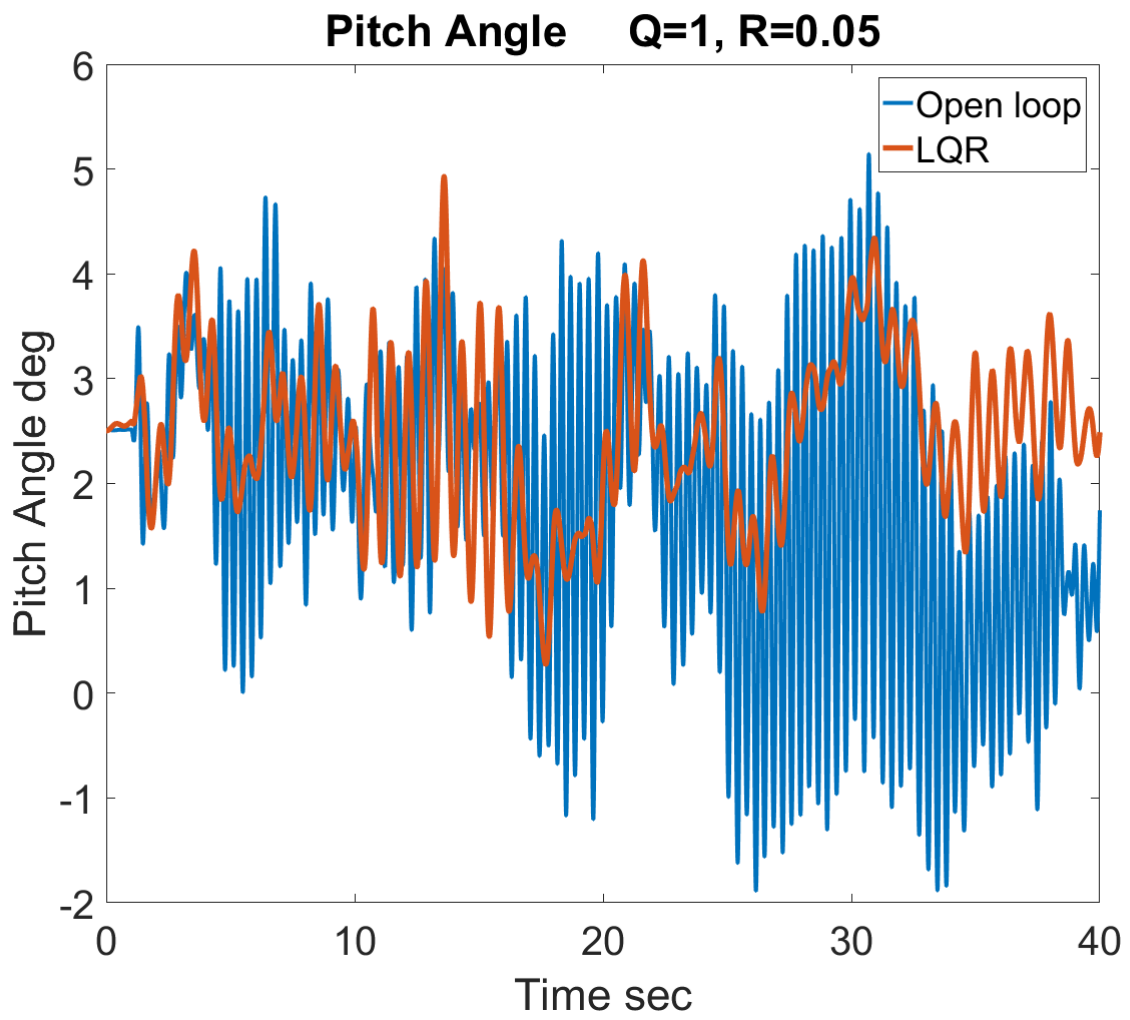


Figure 3.19 Pitch angle for continuous gust at 110m/s

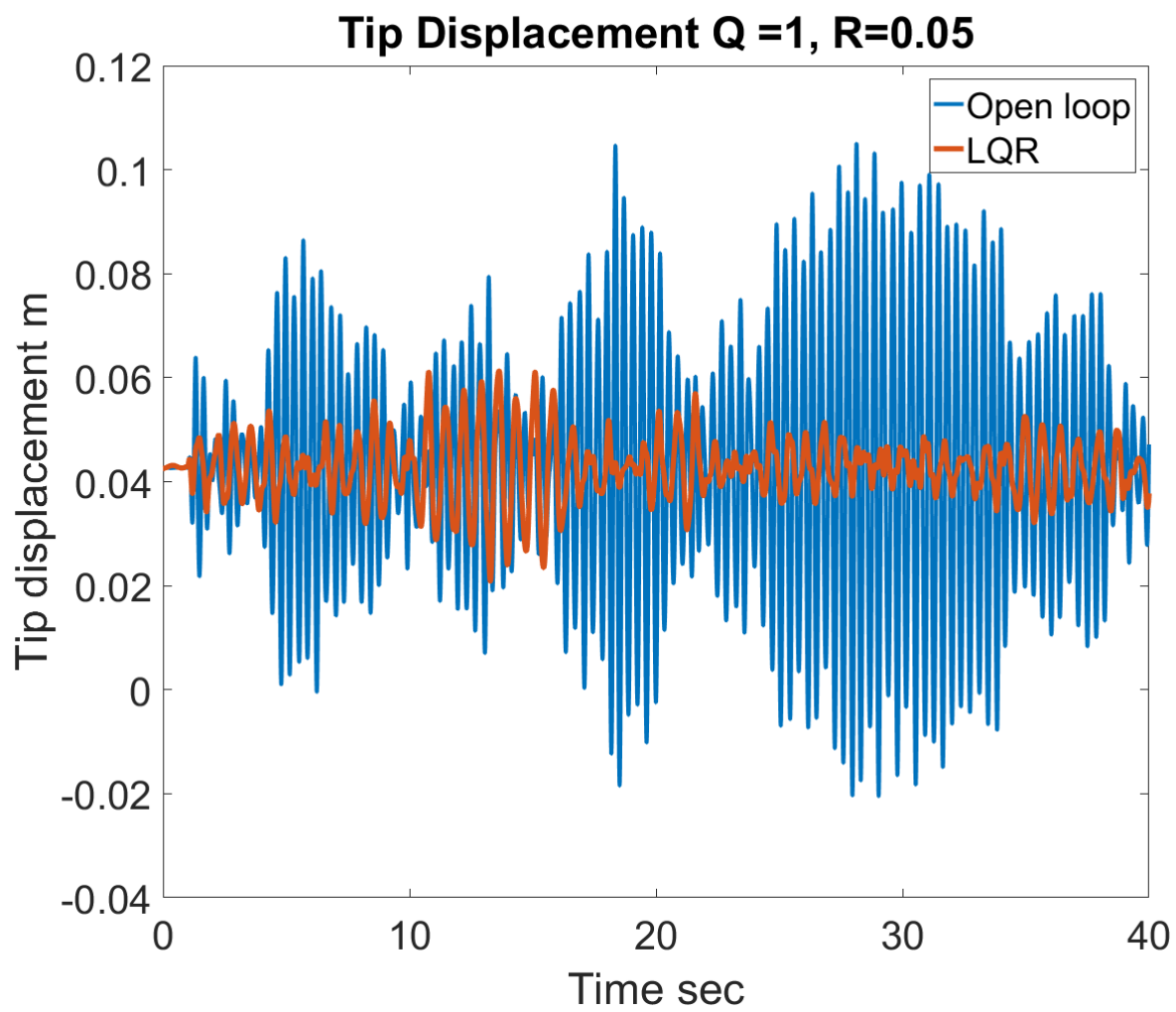


Figure 3.20 Tip displacement for continuous gust at 110m/s

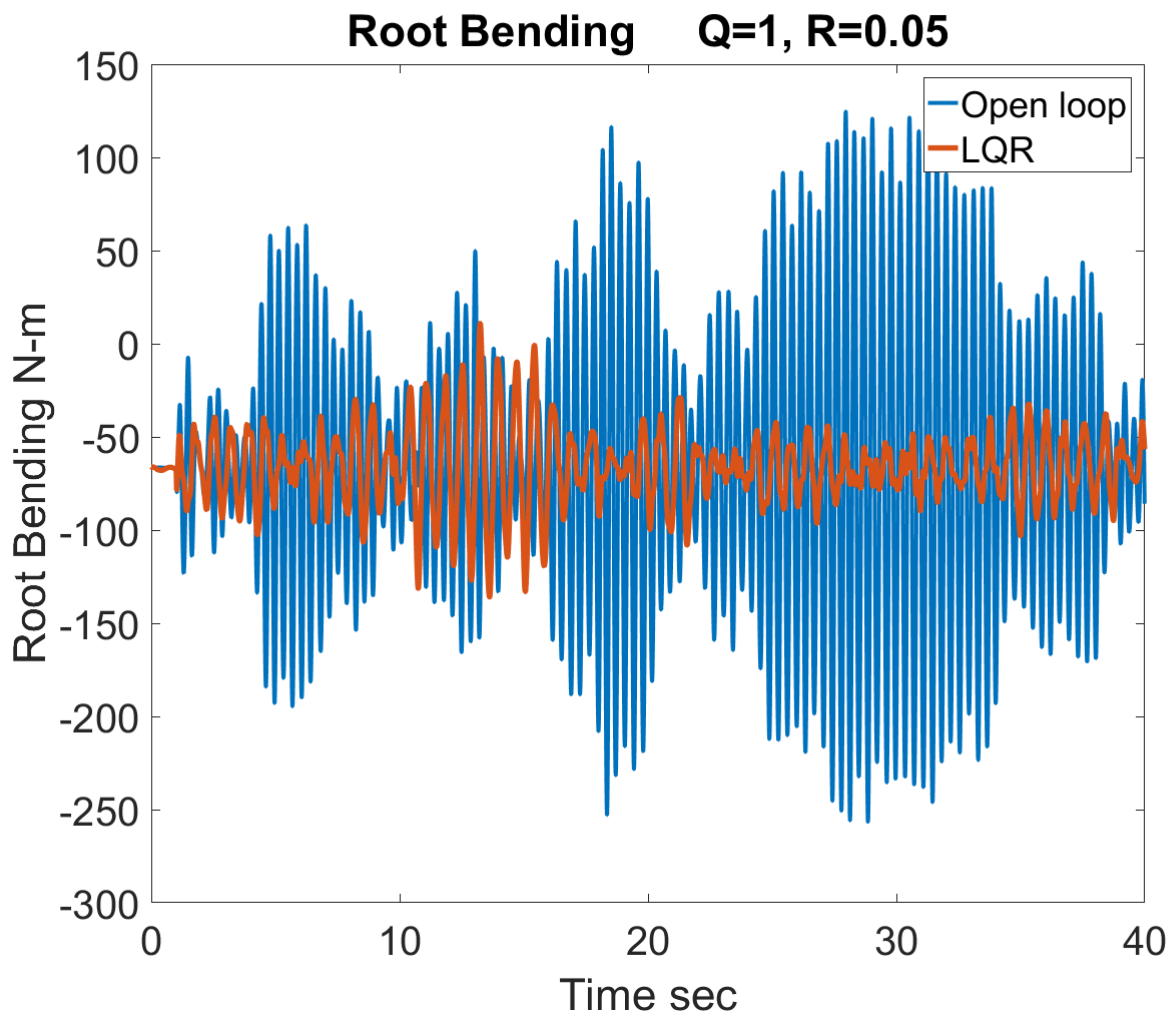


Figure 3.21 Root bending moment for continuous gust at 110m/s

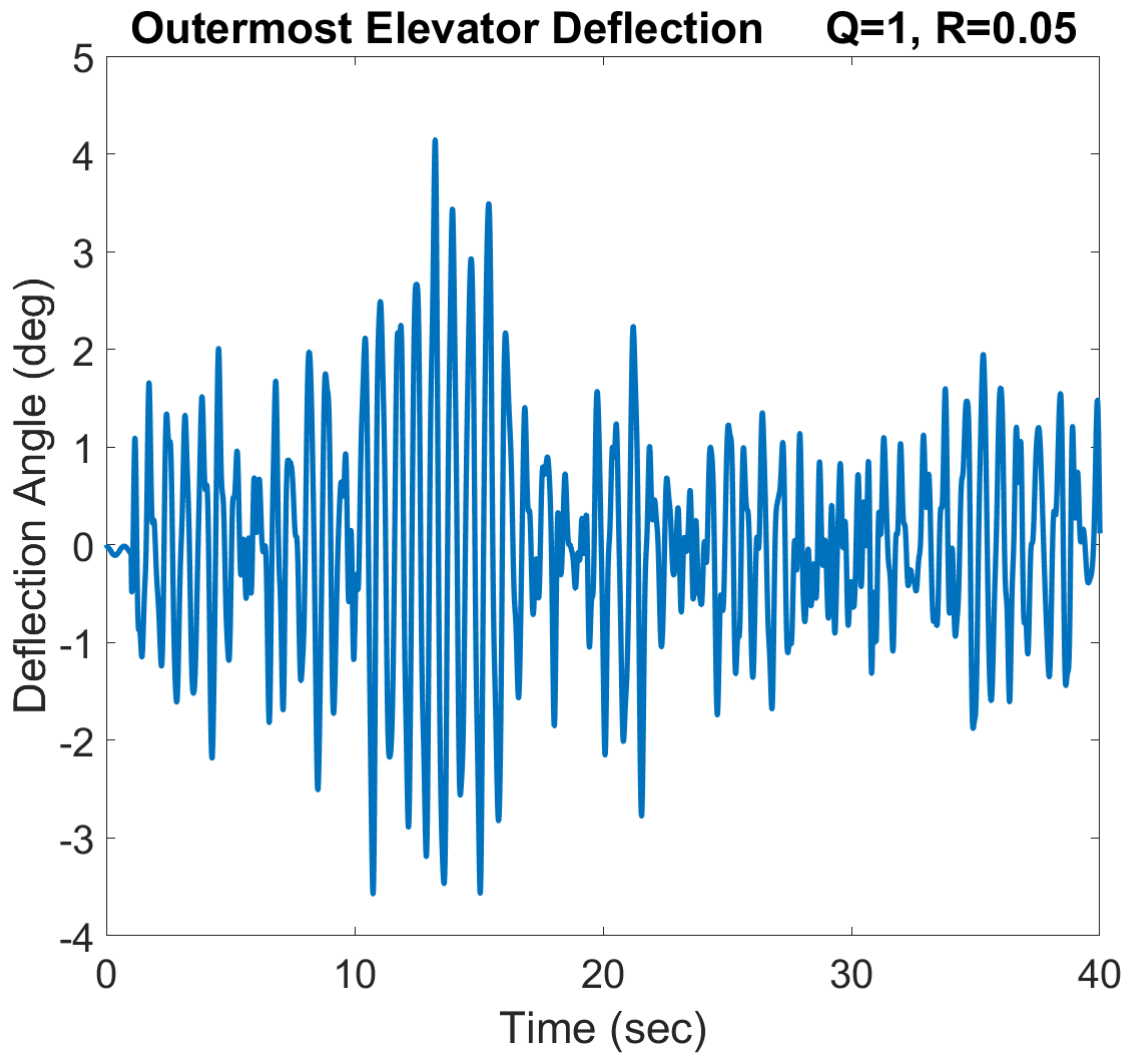


Figure 3.22 Outermost elevator deflection for continuous gust at 110m/s

3.2.3 120 m/s

In a post flutter flight speed with the continuous gust applied, the aircraft enters into a state of instability much quicker than the pre-flutter and nominal flight speeds. As shown in Figure 3.23, the aircraft plunges at a much greater rate than the 110 m/s case. The controller is still able to suppress this instability. The controller is effective in reducing vibration as seen in Figures 3.24 and 3.25 while also reducing the root bending moment of

Figure 3.26 by an order of magnitude. This is comparable performance to the post flutter discrete gust case. The controller is able to prevent the aircraft from becoming unstable at a similar speed with an increase in max amplitude in the gust, although at a cost of very sudden elevator deflections in Figure 3.27.

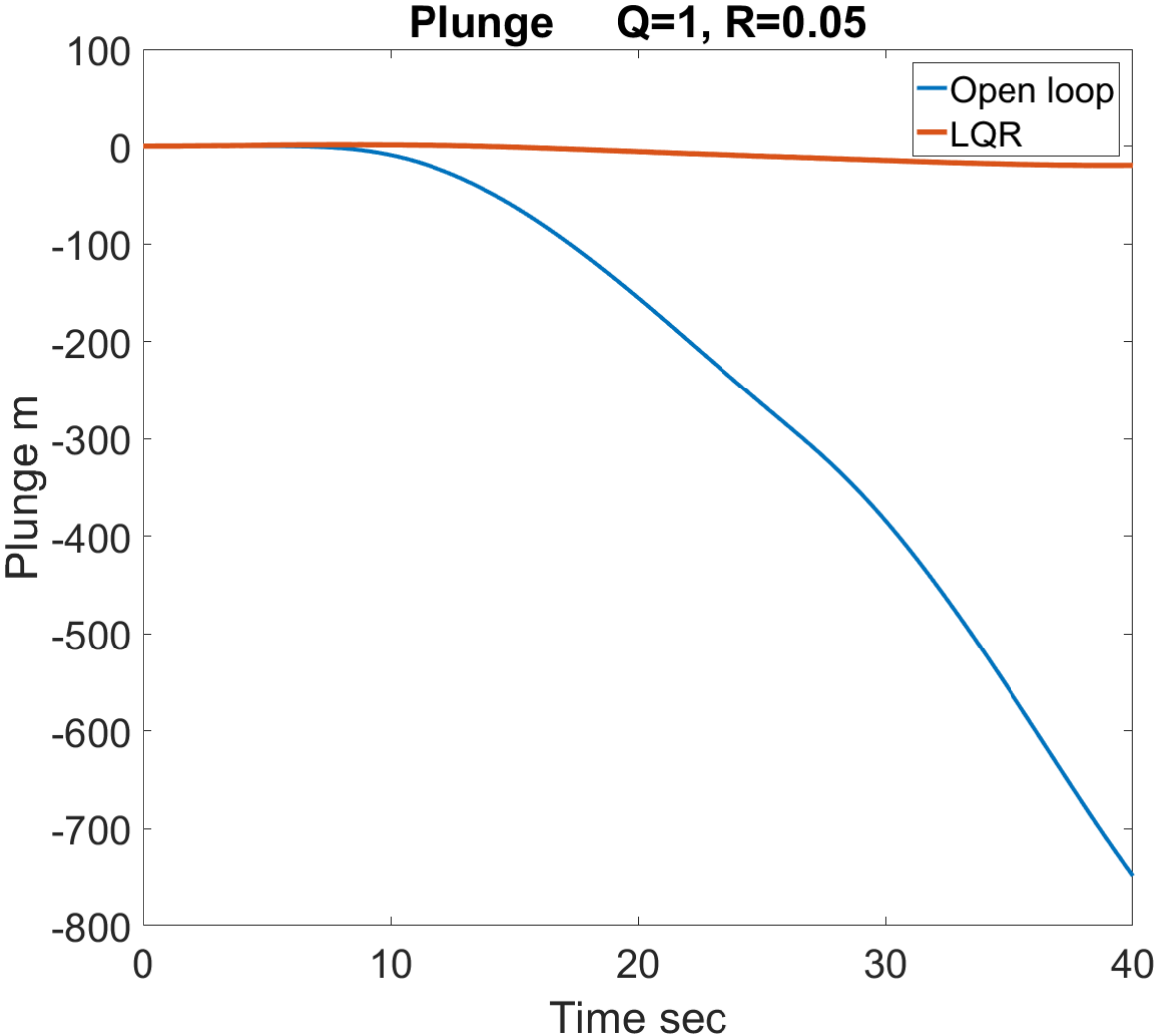


Figure 3.23 Plunge for continuous gust at 120m/s

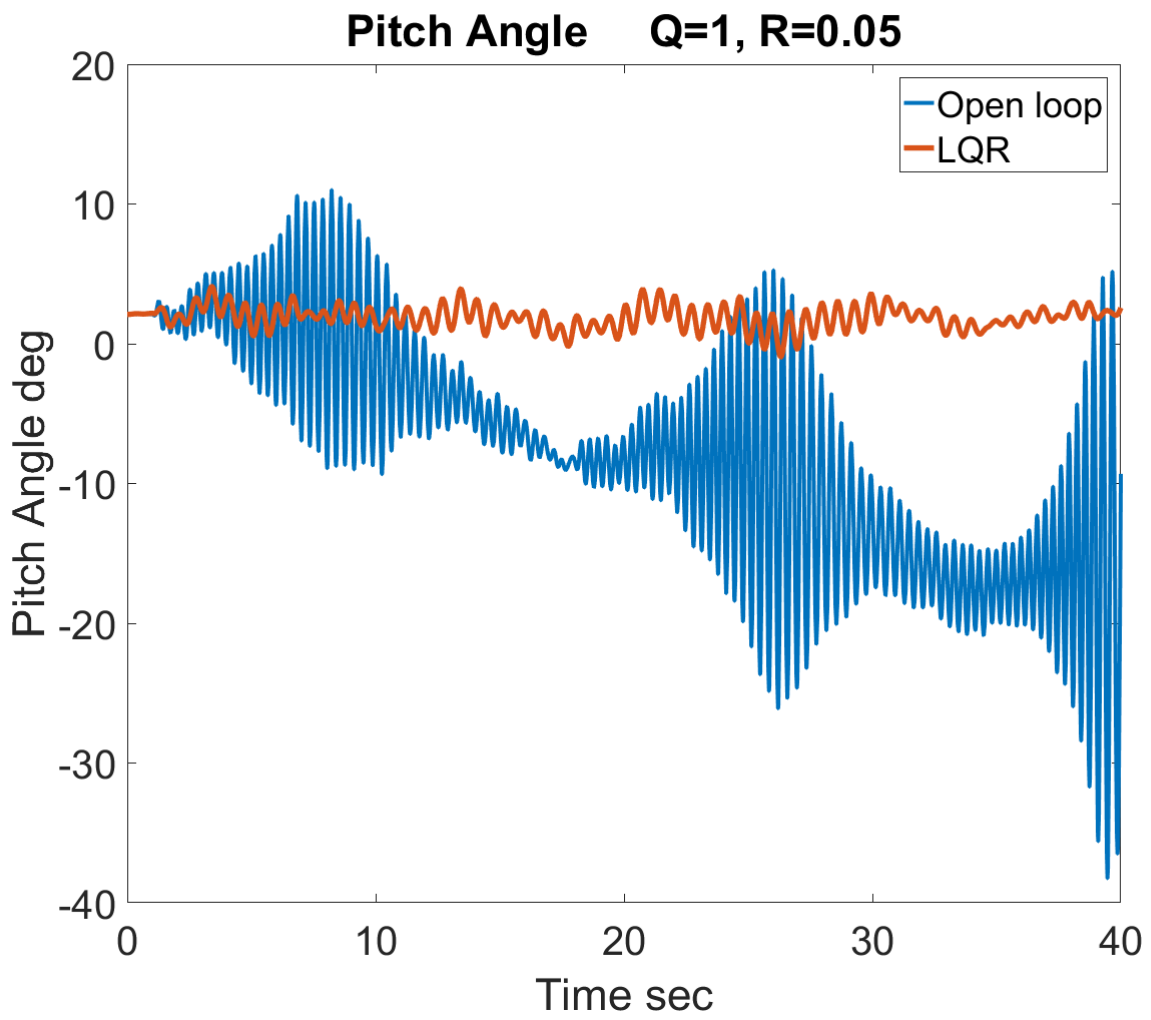


Figure 3.24 Pitch angle for continuous gust at 120m/s

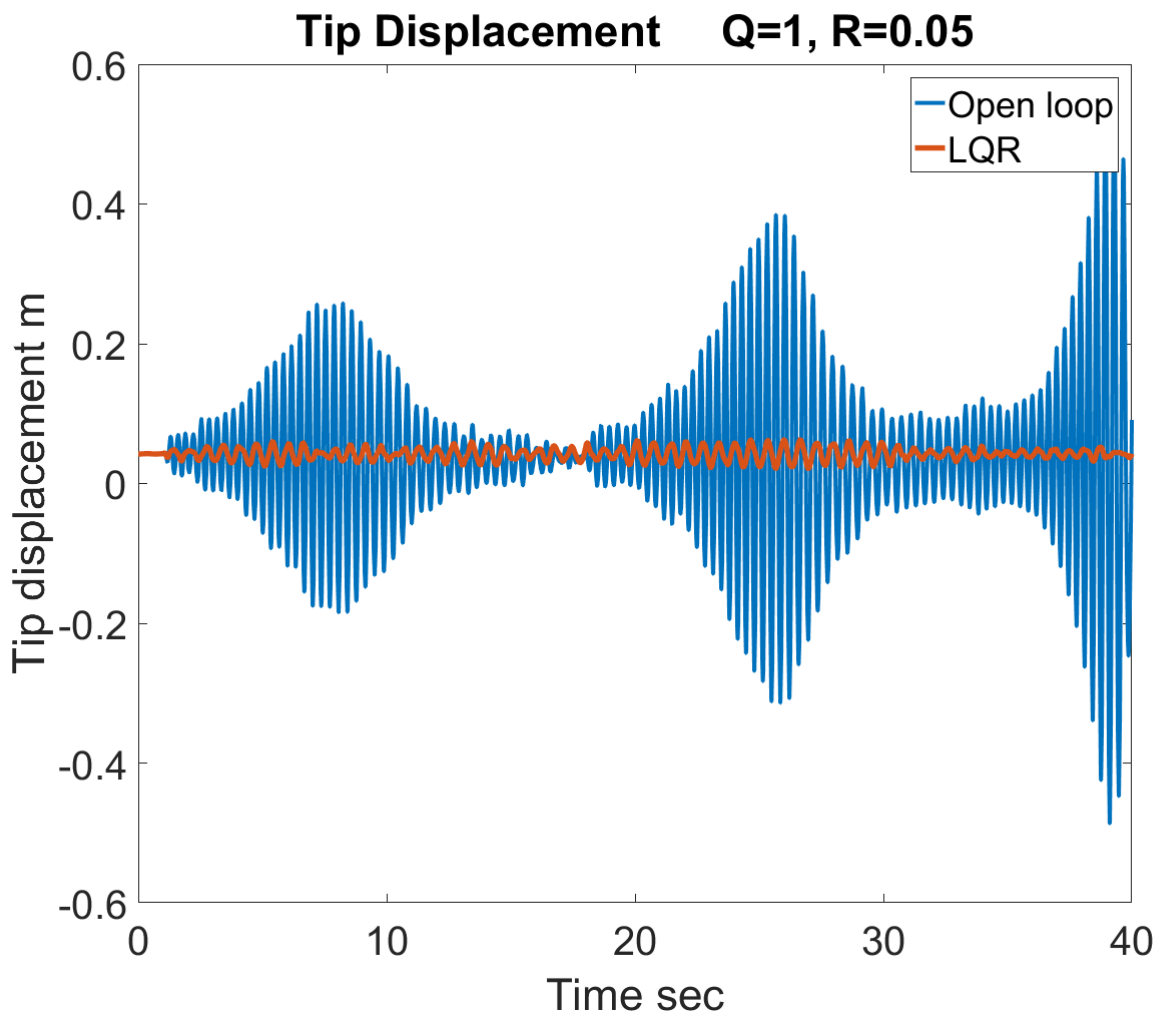


Figure 3.25 Tip displacement for continuous gust at 120m/s

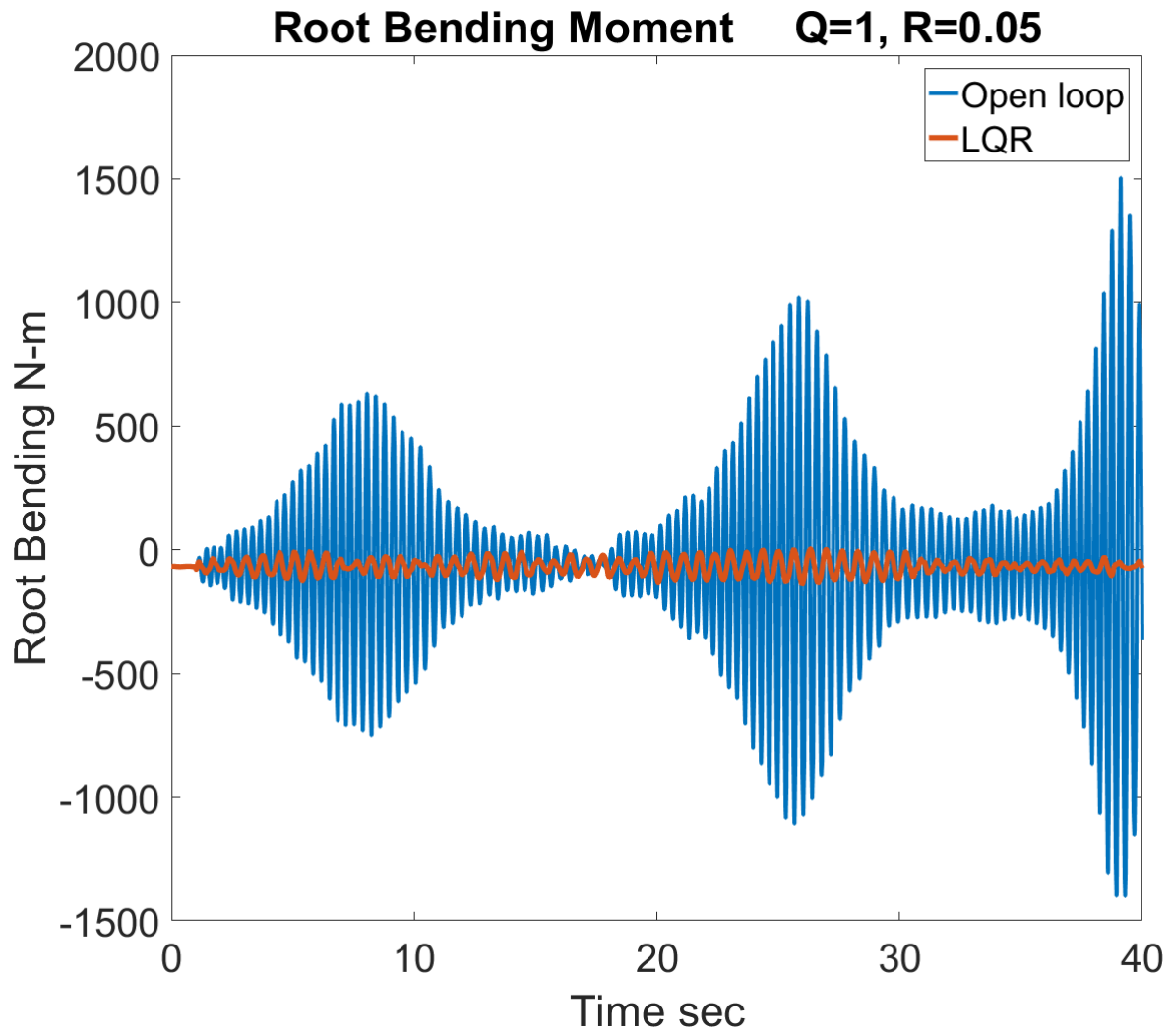


Figure 3.26 Root bending moment for continuous gust at 120m/s

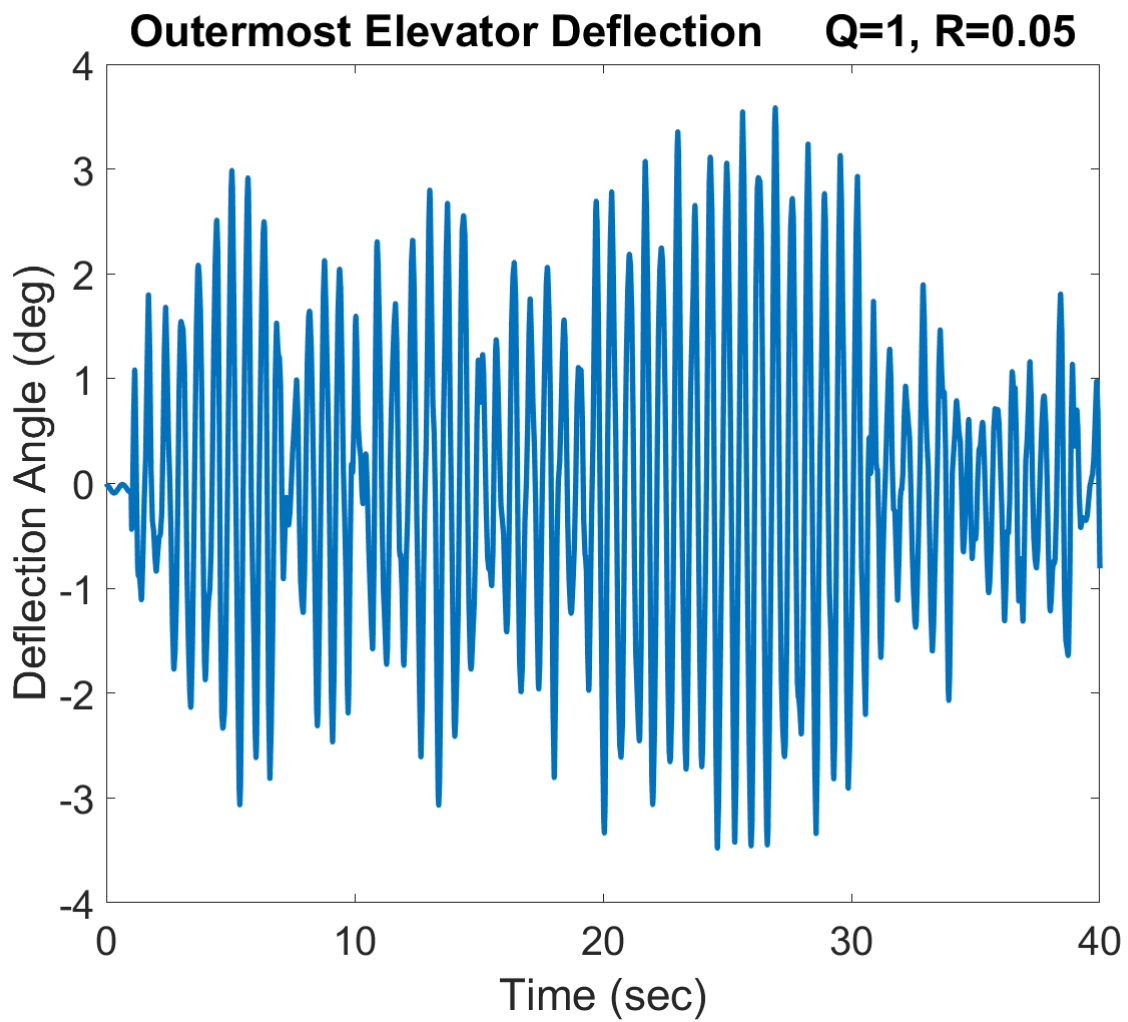


Figure 3.27 Outermost elevator deflection for continuous gust at 120m/s

3.3 No Gust - Post Flutter

This section is used to examine the behavior of the aircraft with no external excitations.

3.3.1 120 m/s

Although the previous cases showed that the aircraft becomes unstable at 120 m/s with a gust, it is still needed to show that the aircraft will experience instability without any other perturbations. Without a gust applied, the aircraft plunges as seen in Figure 3.28 at a higher rate than either gust case. Without any gust applied, the LQR controller performs well, reducing the root bending moment in Figure 3.30 by an order of magnitude and suppressing tip vibration frequency in Figure 3.29. The outermost elevator in Figure 3.31 also experiences minimal deflections throughout the flight profile.

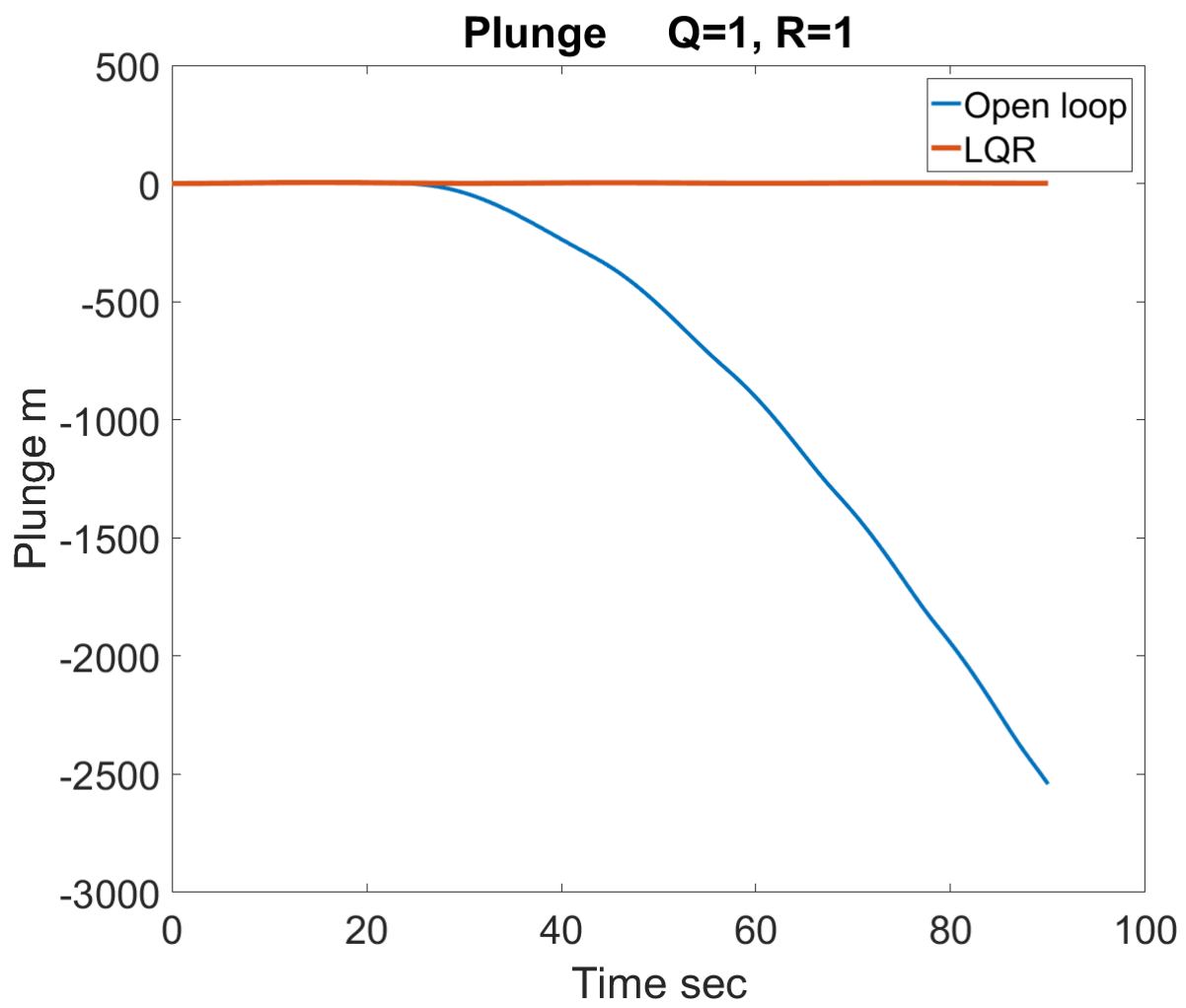


Figure 3.28 Plunge for no gust at 120m/s

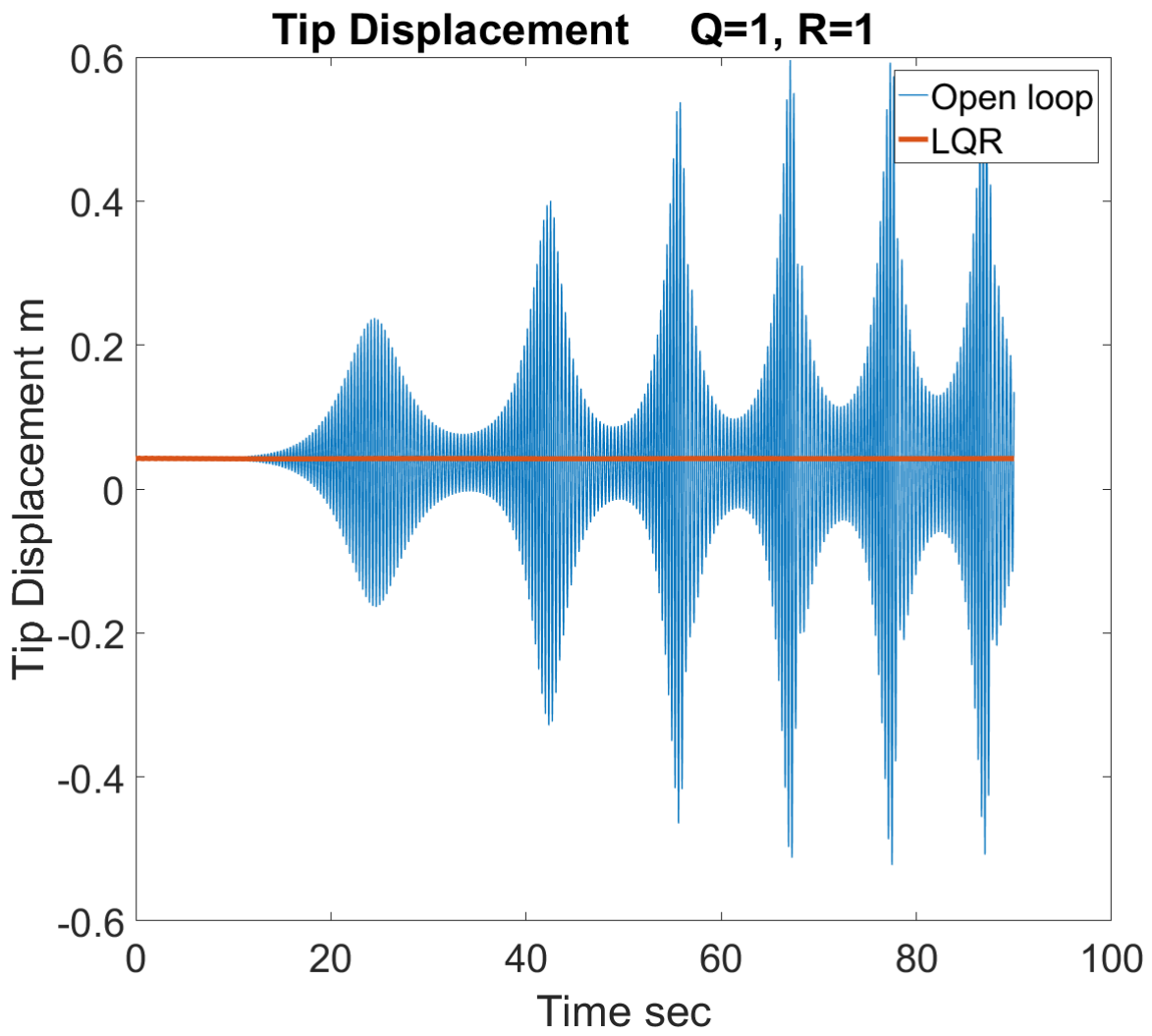


Figure 3.29 Tip displacement for no gust at 120m/s

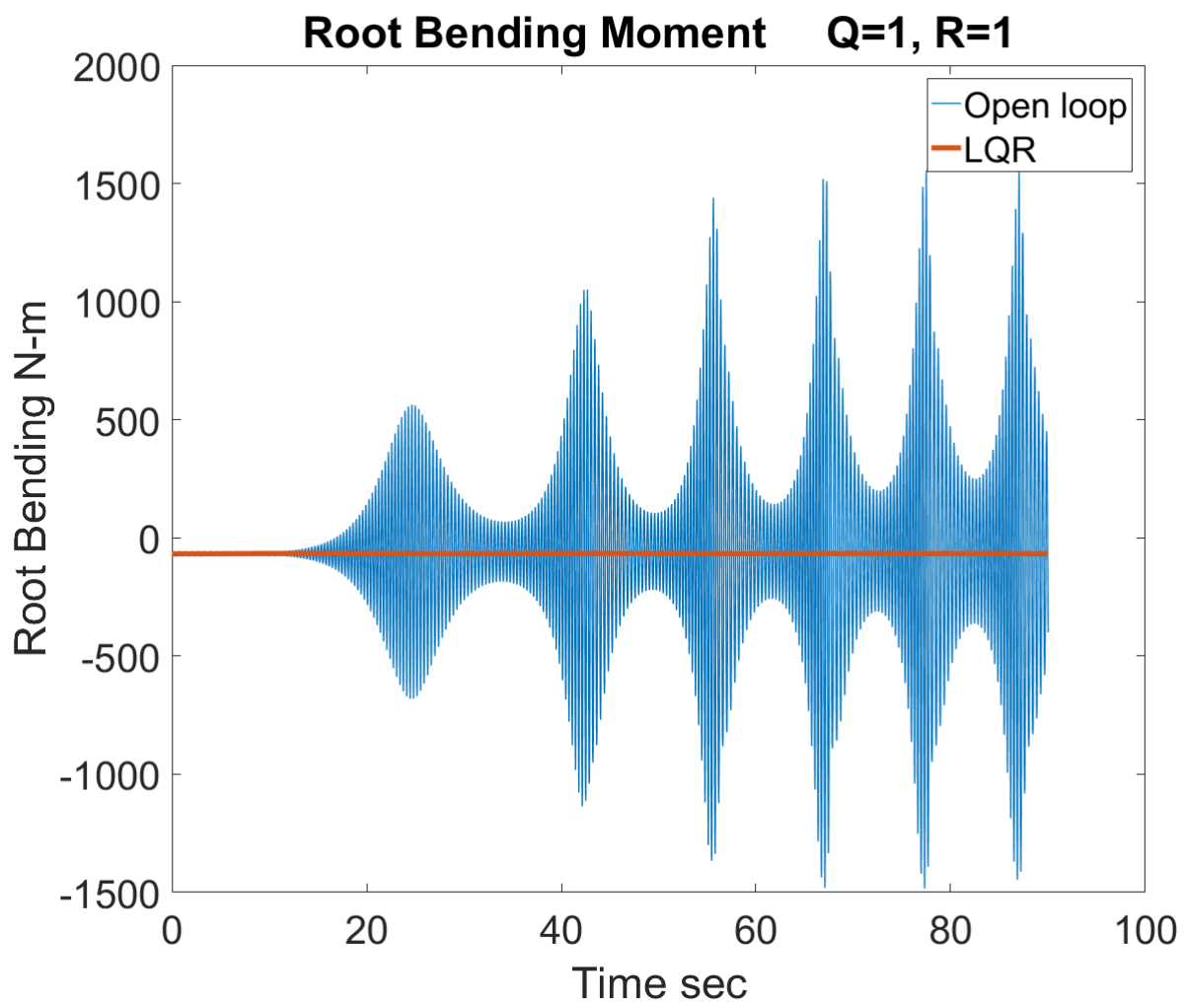


Figure 3.30 Root bending moment for no gust at 120m/s

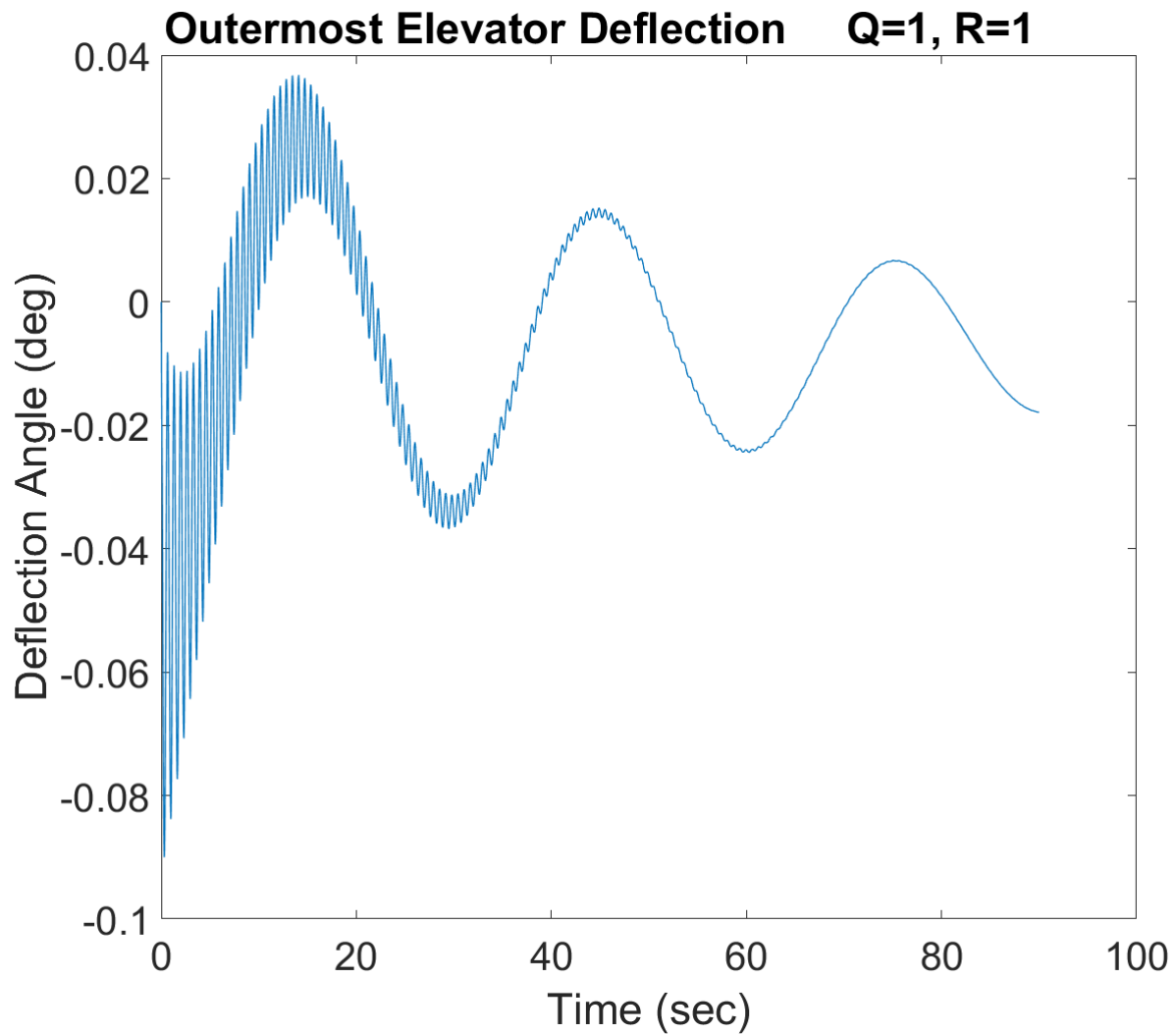


Figure 3.31 Outermost elevator deflection for no gust at 120m/s

3.3.2 125 m/s

The 125 m/s case is post flutter but by 25% instead of the 10% for 120 m/s. This will help test the robustness of the controller by seeing how well it performs far past the flutter boundary. However, Figure 3.32 shows that the controller fails in such an extreme condition. Although the controller reduces the magnitude of the vibration in both the tip

displacement and root bending moment of Figures 3.33 and 3.34, respectively, the closed loop performance is worse than that of the open loop.

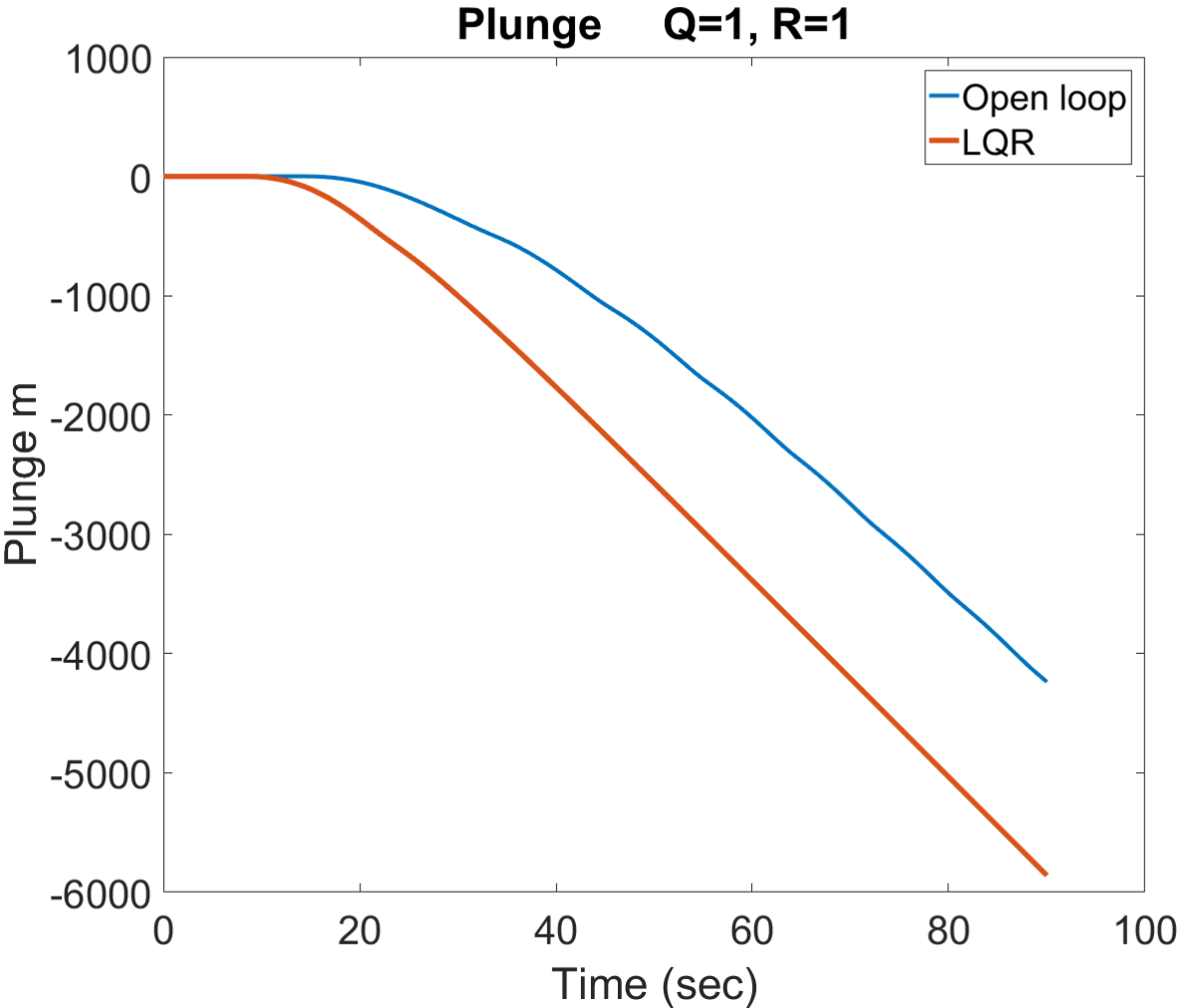


Figure 3.32 Plunge for no gust at 125m/s

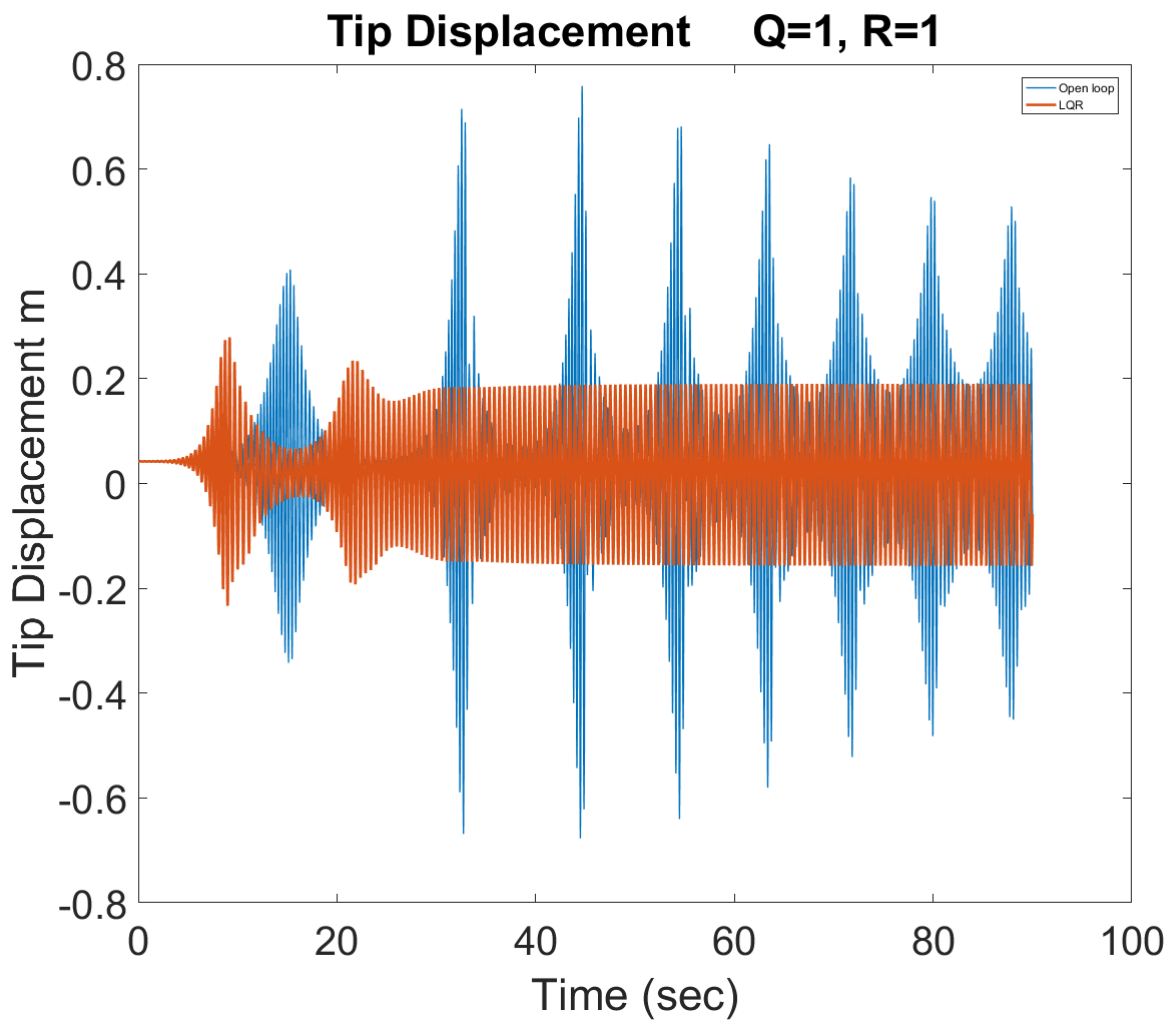


Figure 3.33 Tip displacement for no gust at 125m/s

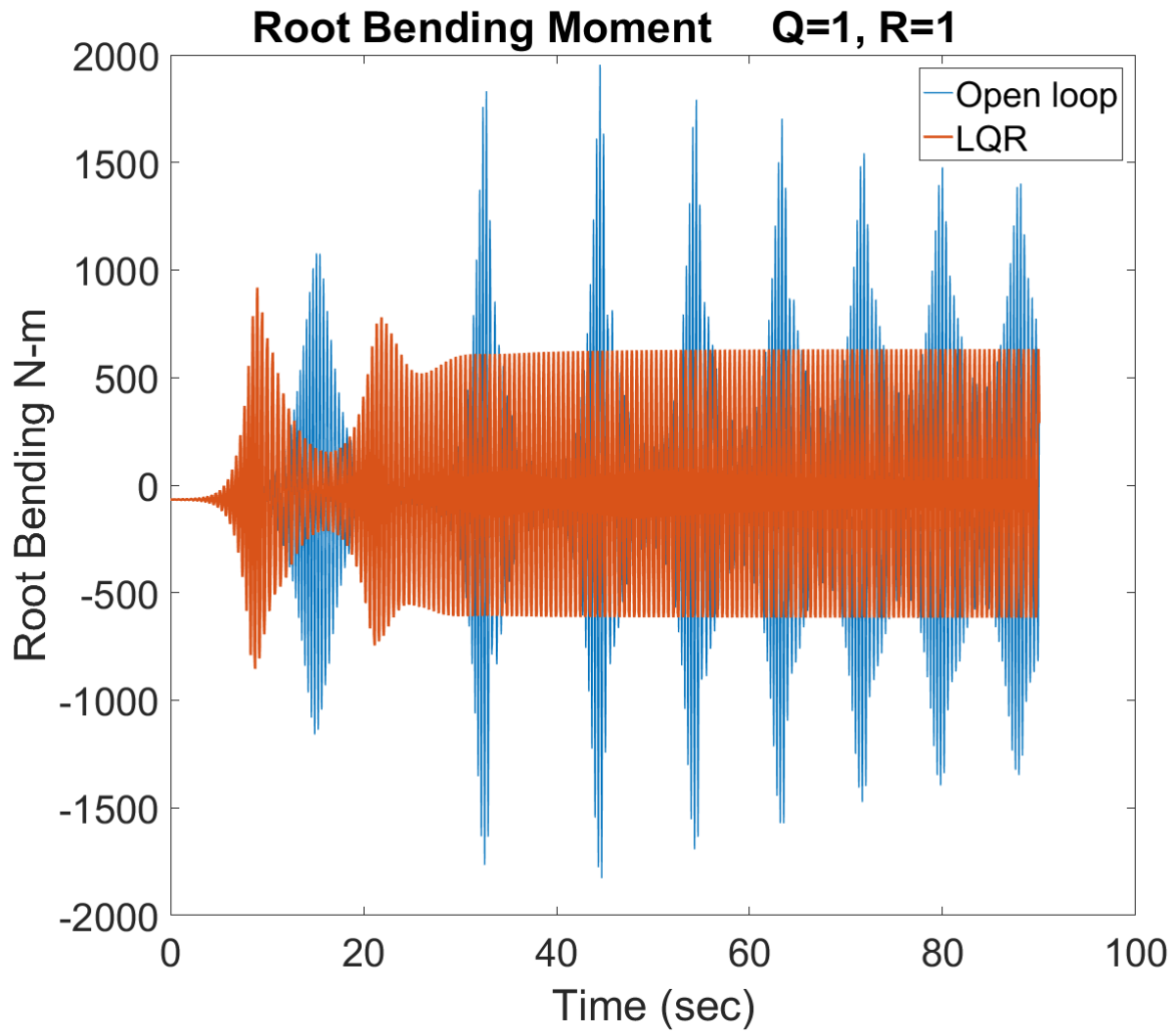


Figure 3.34 Root bending moment for no gust at 125m/s

4 CONCLUSION AND FUTURE WORK

4.1 Conclusions

The ability of an LQR controller to suppress vibration of a blended-wing-body aircraft subjected to gusts was explored in this thesis. Initially, the aircraft was trimmed at each flight speed. The LQR controller was then implemented and tested in a nonlinear framework. The aircraft was examined in three cases: a discrete gust, a continuous gust, and post-flutter free flight. For the discrete and continuous gust cases, nominal (90 m/s), pre-flutter (110 m/s), and post flutter (120 m/s) flight speeds were used. The free flight case was examined at 10% and 25% past the flutter boundary.

The controller aimed to minimize the strain and strain rate states within each element of the aircraft as it experienced two gust profiles in a range of speeds. Although the rigid body states would need to be included in the control design for a conventional aircraft, the inherent nature of the blended wing body design allows for the rigid body motion and strains to be coupled. Thus, reducing the strains and strain rates would implicitly reduce the rigid body motion. This can be seen in the controller's ability to stabilize the plunge motion with some gust excitations. The controller showed effectiveness at lower speeds and seemed to perform best at the post flutter speed, reducing the wing's root bending moment by an order of magnitude lower than the open loop case. The two different gust profiles did not seem to affect the performance of the

controller. That is, the controller did not have difficulties reducing vibrations from an initial disturbance or a continuous disturbance.

Although the controller was successful in suppressing vibrations within the aircraft, it should be noted that the weighting matrices Q and R were in no way optimized. The effects of this can be seen in the continuous gust case at 90 m/s. The controller did reduce the frequency but did not reduce the magnitude of the aircraft's pitch angle. The controller was also designed without any state and input coupling, N . The controller also has a consistent issue with large, immediate elevator inputs. A smoothing function would need to be developed and implemented in order to reduce the sudden jumps from -8 to 8 degrees. The limitation of the controller was also shown at 25% past the flutter boundary, 125 m/s for this aircraft. It is unknown whether this could be pushed back farther if the controller was optimized in some way or if the state and input coupling term was included.

4.2 Future Work / Recommendations

This paper has shown the feasibility of using an LQR controller in a nonlinear framework for a blended wing body aircraft. Going forward, research may need to be done on optimizing the controller in some way. Implementing a more robust control scheme, allowing for multiple flight conditions instead of the cruise conditioned examined in this paper. In the actual aircraft, not all of the states will be known. A Linear-quadratic-Gaussian control design may be needed to account for the missing states.

REFERENCES

- [1] Yagil, L., Raveh, D. E., and Idan, M., "Deformation Control of Highly Flexible Aircraft in Trimmed Flight and Gust Encounter," *Journal of Aircraft*, vol. 55, 2018, pp. 829–840.
- [2] "Finite state aeroelastic model for use in rotor design optimization," *Journal of Aircraft*, vol. 30, 1993, pp. 777–784.
- [3] Dillsaver, M., Cesnik, C., and Kolmanovsky, I., "Gust Load Alleviation Control for Very Flexible Aircraft," AIAA Atmospheric Flight Mechanics Conference, 2011.
- [4] Heredia, A. I. D., and Friehmelt, H., "GN&C Concepts for a Blended Wing Body," AIAA Guidance, Navigation, and Control Conference and Exhibit, 2005.
- [5] Wildschek, A., "Flight Dynamics and Control Related Challenges for Design of a Commercial Blended Wing Body Aircraft," AIAA Guidance, Navigation, and Control Conference, 2014.
- [6] Su, W., and Cesnik, C. E. S., "Dynamic Response of Highly Flexible Flying Wings," AIAA Journal, vol. 49, 2011, pp. 324–339.
- [7] Hammerton, J. R., Su, W., Zhu, G. G., and Sweil, S. S.-M., "Optimum Wing Shaping and Gust Load Alleviation of Highly Flexible Aircraft with Finite Actuators," 2018 AIAA/ASCE/AHS/ASC Structures, Structural Dynamics, and Materials Conference, 2018.
- [8] Su, W., and Tsushima, N., "Modeling of Highly Flexible Multifunctional Wings for Energy Harvesting," 56th AIAA/ASCE/AHS/ASC Structures, Structural Dynamics, and Materials Conference, 2015.
- [9] Magar, K. S. T., Reich, G. W., Pankonien, A. M., and Smyers, B., "Active Gust Alleviation using Artificial Hair Sensors and Feedforward Control," AIAA Guidance, Navigation, and Control Conference, 2017.

- [10] Su, W., and Cesnik, C. E. S., "Nonlinear Aeroelasticity of a Very Flexible Blended-Wing-Body Aircraft," *Journal of Aircraft*, vol. 47, 2010, pp. 1539–1553.
- [11] Köthe, A., Luckner, R., Ramirez, P. J. G., Silvestre, F. J., Pang, Z. Y., and Cesnik, C. E., "Development of Robust Flight Control Laws for a Highly Flexible Aircraft in the Frequency Domain," AIAA Atmospheric Flight Mechanics Conference, 2016.
- [12] He, T., Zhu, G. G., Swei, S. S.-M., and Su, W., "Smooth-switching LPV control for vibration suppression of a flexible airplane wing," *Aerospace Science and Technology*, vol. 84, 2019, pp. 895–903.
- [13] Yost, J. D., Jackson, W. B., and Salter, L. W., "Improved Methods of Atmospheric Turbulence Prediction for Aircraft Design and Operation J," *Journal of Aircraft*, vol. 9, 1972, pp. 266–272.
- [14] Campbell, C., and Maciejowski, J., "Control and Guidance of a Highly-Flexible Micro Air Vehicle Using Model Predictive Control," AIAA Guidance, Navigation, and Control Conference, 2009.
- [15] Patil, M. J., Hodges, D. H., and Cesnik, C. E. S., "Nonlinear Aeroelasticity and Flight Dynamics of High-Altitude Long-Endurance Aircraft," *Journal of Aircraft*, vol. 38, 2001, pp. 88–94.
- [16] Su, W., and Cesnik, C. E. S., "Strain-Based Analysis for Geometrically Nonlinear Beams: A Modal Approach," *Journal of Aircraft*, vol. 51, 2014, pp. 890–903.